Chapter 33

Polybenzoxazine-Based Nanofibers by Electrospinning

Y. Ertas and T. Uyar[1]
Bilkent University, Ankara, Turkey
[1]Corresponding author: e-mail: uyar@unam.bilkent.edu.tr

Chapter Outline

1 INTRODUCTION

Polybenzoxazine is a new, developing phenolic-type thermoset resin that has attracted much attention in recent years because of its outstanding properties, and the different forms of polybenzoxazine (such as bulk [1–5], film [6–19], aerogel [20–25], and porous membranes [26,27]) and their various applications have been studied extensively. At the same time, production of nanofibers from polybenzoxazine resins and incorporation of the polybenzoxazines into the other polymeric nanofibers for the functionalization and enhancement of the existing properties is a developing area.

Polybenzoxazines have been used recently for the superhydrophobic surface modification of polymeric nanofibrous membranes [28–30]. Until now, various approaches, such as plasma treatment, chemical deposition, colloidal assembly, lithography, and template-based techniques, have been employed to produce superhydrophobic membranes [31–34]. However, such functional membranes are still limited in terms of large-scale production and practical applications because of expensive and complicated fabrication procedures, harsh practical conditions, and low stability and flexibility, as well as poor selectivity and recyclability. On the other hand, electrospinning is a simple but powerful technique for preparing functional fibrous membranes at nanoscale and microscale levels from a variety of polymers, polymer blends, sol-gels, composites, and ceramics [35,36]. Moreover, nanofibers produced by electrospinning have several significant features, such as a very large surface area to volume ratio and nanoscale pores. In addition, materials with a nanofibrous structure exhibit distinctive chemical, physical, and mechanical properties when compared to their bulk or film forms. The unique properties and multifunctionality of such nanofibrous structures are suitable for use in a variety of areas and systems, including healthcare, filtration/membrane, textiles, environmental, energy, electronics, and sensors [35–41].

Surface modification of such functional membranes with hierarchical rough surfaces and controlled wettability provide the fabrication of superhydrophobic membranes [32,42]. It is well known that polybenzoxazine is an addition polymerized phenolic system with low surface energy and that it can induce hydrophobicity and oleophilicity along

Advanced and Emerging Polybenzoxazine Science and Technology. http://dx.doi.org/10.1016/B978-0-12-804170-3.00033-0

with a wide range of interesting features, including near-zero volumetric change upon curing, chemical resistance, low water absorption, and high glass-transition temperature, which all make it a promising component for functional membranes with special wettability [43–45]. Although it has been known for some time that superhydrophobic spin coating can be prepared from polybenzoxazine [45,46], until recently very few studies reported on the development of flexible polybenzoxazine–modified nanofibrous membranes especially for oil-water separation. Selective adsorption of the oil from oil-water mixtures generally depends on the hydrophobicity and oleophilicity of the membrane surface. The wettability of solid surfaces is generally controlled by their surface chemistry and geometrical roughness [47–49]. Basically, the introduction of a proper roughness can make a smooth hydrophobic surface more hydrophobic or even superhydrophobic because of air being trapped under the water droplets as a cushion; on the other hand, an oleophilic surface becomes more oleophilic or even superoleophilic because of the capillary effect [50–53]. Also, the incorporation of benzoxazine precursors into the polymeric nanofibers is another way to obtain superhydrophobic surfaces because polybenzoxazines are low-surface-free-energy polymeric materials.

Another interesting application of polybenzoxazine is its use as a precursor for the production of magnetic carbon nanofibers (MCNFs). Traditionally, synthetic approaches—such as a substrate method, a spraying method, a vapor growth method, and a plasma-enhanced chemical vapor deposition method—are used for the fabrication of CNFs. However, not only are these methods complicated and costly, they also are not suitable for the production of Fe_3O_4 nanoparticle (NP)–embedded porous MCNFs because it is difficult to increase the pore volume and mass fraction of Fe_3O_4 [54]. On the other hand, electrospinning is a simple and inexpensive method for producing nanoscale and mesoscale 1D composite nanofibers from a combination of organic and inorganic precursors [34,55]. Through the calcination of these electrospun precursor nanofibers, MCNFs can be produced [56]. On principle, the nature of the precursor nanofibers strongly affects the structural properties of electrospun MCNFs, because internal and surface defects of the precursor nanofibers can be transferred easily into the obtained MCNFs, causing performance to deteriorate [57]. Polyacrylonitrile (PAN) is the most commonly used precursor polymer for the production of electrospun CNFs [58]. Moreover, pitch, poly(vinyl alcohol), poly(vinylidene fluoride), poly(methyl methacrylate), poly(vinyl pyrrolidone), and poly(*p*-xylene tetrahydrothiophenium chloride) have also been reported [54,59–61]. However, in order to convert these thermoplastic polymers into highly condensed thermosetting fibers and at the same time prevent the fibers from fusing together during carbonization, a time-consuming and expensive stabilization process is required, which limits the practical use of these electrospun CNFs [54]. On the other hand, the interesting features of polybenzoxazine—such as near-zero volumetric change during curing, higher glass-transition temperature, and high char yield [43,45,62]—suggest that it is a promising precursor for high-performance CNFs.

In addition to the means just discussed, via electrospinning, suitable polybenzoxazine molecules can be synthesized because of the flexibility of their molecular design in order to produce polymer-free, completely polybenzoxazine–based nanofibers. Because chain entanglement and overlapping play vital roles in the formation of nanofibers during electrospinning, main-chain polybenzoxazines (MCPBz) with a chain structure can be synthesized from difunctional phenolic derivatives and difunctional primary amines. By combining the properties of polybenzoxazines and the features of electrospun nanofibers highly cross-linked thermoset polybenzoxazine nanofibrous mat, which has good mechanical/thermal properties and high stability in harsh environmental conditions, can be obtained. In addition, because of the cross-linked Mannich bridge structure with benzene rings all over the fibers and the roughness provided by the nanoscale fibrous structure, these materials possess inherent hydrophobic characteristic, without further surface modification. Therefore these materials are quite useful for filtration systems that require high temperatures and that are often in harsh environmental conditions.

2 SURFACE MODIFICATION OF NANOFIBROUS MEMBRANES BY IN SITU POLYMERIZATION OF BENZOXAZINES

2.1 Superhydrophobic Silica Nanofibrous Membrane by In Situ Polymerization of Benzoxazine

Yang and coworkers fabricated superhydrophobic membranes by in situ polymerization of fluorinated polybenzoxazine incorporating SiO_2NPs on silica nanofibrous membrane (SNM), which is produced by calcination (800°C) of electrospun tetraethylorthosilicate/poly(vinyl alcohol) composite nanofibers (Fig. 1) [28]. Here novel bifunctional fluorinated benzoxazine (HID-tma) synthesized from 4,4′-(hexafluoroisopropylidene) disphenol, *m*-(trifluoromethyl) aniline and paraformaldehyde was used as the starting monomer. The SNM were modified by dipping in various concentrations of a HID-tma solution and then were dried in an oven for 20 min at 60°C. Subsequently, in situ polymerization of HID-tma was carried out at 190°C in a vacuum oven for 1 h yielding the formation of poly(HID-tma) on the SNM surfaces. In addition, the hydrophobicity of the SNM were regulated by introducing the different concentrations of the SiO_2NPs (0.1, 0.5, 2, and 3 wt%) into the HID-tma solutions

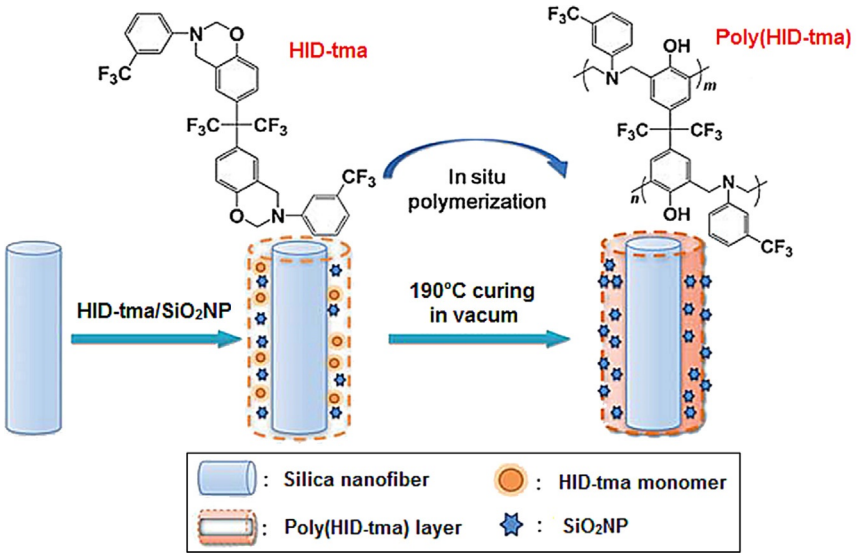

FIG. 1 Illustration showing the synthesis procedure of poly(HID-tma)/SiO_2NP/SNM and the relevant formation mechanism [28].

(0.001, 0.05, 0.5, and 2 wt%) and then in situ polymerization was carried out as before. The relevant poly(HID-tma)/SiO_2NP–modified SNM were denoted as poly(HID-tma)-*x*/SiO_2NP-*y*/SNM, where *x* is the concentration of HID-tma (*x* wt%) and *y* is the concentration of SiO_2NPs (*y* wt%).

SNM has numerous silanol (Si-OH) groups on the fibers' surfaces, which provides perfect contact with water droplets because of the strong hydrogen bonding, thus showing superhydrophilic characteristics with a water contact angle (WCA) of 0 degree and a oleophilic characteristic with an oil contact angle (OCA) of 22 degrees. First, the surface chemistry of the SNM was altered by dipping the HID-tma solutions and by a subsequent curing at 190°C. In this step, HID-tma was polymerized through ring-opening and cross-linking reactions and yielded a thermoset poly(HID-tma) layer on the fiber surface, which shows a hydrophobic characteristic because of the highly cross-linked Mannich bridge structure with benzene rings. Poly(HID-tma)–modified SNM exhibited promising hydrophobicity (142 degrees) up to a 2 wt% concentration; however, a further increase in the concentration of HID-tma (4 wt%) caused the formation of film among the nanofibers, thus reducing the roughness of the membranes and decreasing the WCA to about 133 degrees.

Wenzel and Cassie-Baxter described two equilibrium configurations for superhydrophobic rough surfaces, as wetted state and non-wetted state, respectively [50,51]. At wetted state, the liquid was in contact with the whole solid surface under it; at non-wetted state, the liquid was in contact with only the top part of the rough surface. These two models suggest mechanisms for the effect of roughness on the static WCA when the water droplet rest on the rough surface with minute hysteresis. They also suggest that surface modification with suitable multiscale roughness makes the hydrophobic surface more hydrophobic and the oleophilic surface more oleophilic. Therefore the incorporation of 0.1, 0.5, 2, and 3 wt% SiO_2NP into the 0.5 wt% HID-tma remarkably increased the surface roughness, and the WCA of the membranes were measured as 146, 151, 161, and 158 degrees, respectively (Fig. 2). However, a further increase of the SiO_2NP content to 3 wt% would cause the aggregation of NPs on the nanofibers as well as among the spaces between the nanofibers, resulting in a slight decrease of WCA, as shown in Fig. 2. The resultant poly(HID-tma)-0.5/SiO_2NP-2/SNM with fine hierarchical roughness showed the highest WCA at 161 degrees and the lowest sliding angle at 4 degrees.

Poly(HID-tma)-0.5/SNP-2/SNM membrane showed robust thermal stability upon high-temperature treatment. This membrane exhibited superhydrophobicity until 250°C and maintained good hydrophobicity of 135 degrees even after a heat treatment of 450°C. Also, as-prepared poly(HID-tma)-0.5/SiO_2NP-2/SNM has shown favorable bending and recovering behaviors, revealing excellent flexibility with no crack formation during the process (Fig. 3A). Moreover, a KES multipurpose bending test (KES-FB2S) was carried out on the SNM, poly(HID-tma)-0.5/SNM, and poly(HID-tma)-0.5/SiO_2NP-2/SNM for further characterizations of the flexibility of the membranes (Fig. 3B). The corresponding bending rigidities based on the Grosberg's model [63] were 0.0085, 0.0215, and 0.0127 gf cm, respectively, implying good flexibility for all the three samples. In addition, mechanical properties of the SNM, poly(HID-tma)-0.5/SNM, and poly(HID-tma)-0.5/SiO_2NP-2/SNM were investigated by a typical stress strain curve. The membranes showed similar robust tensile strengths of 2.64, 2.46, and 2.58 MPa, respectively, indicating that the fluorinated polybenzoxazine modification does not affect the tensile strength of membranes. Also, all the membranes exhibited a nonlinear elastic behavior at first under a stress load,

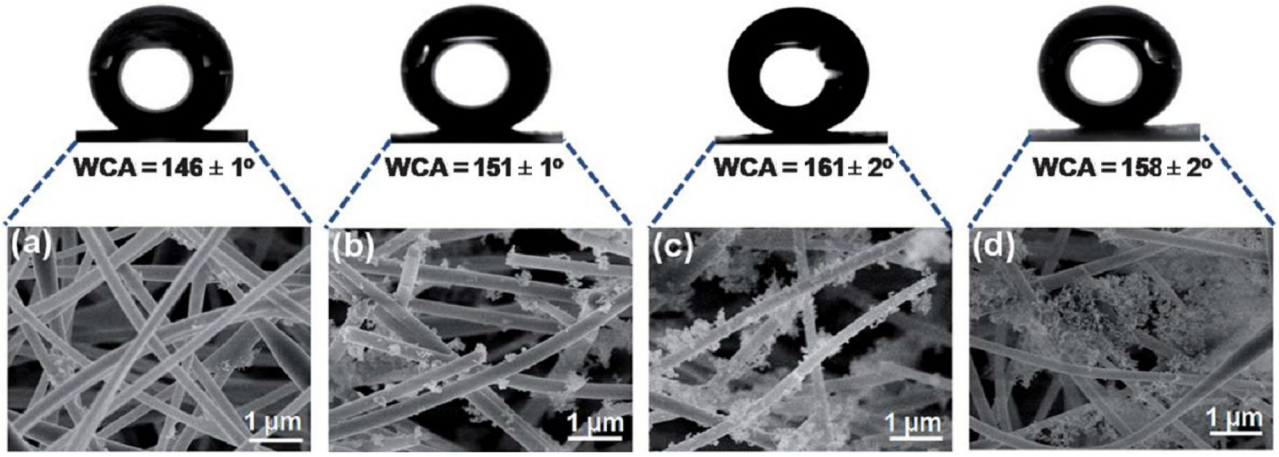

FIG. 2 Field emission scanning electron microscopy (FE-SEM) images and the corresponding optical profiles of water droplets of (A) poly(HID-tma)-0.5/SiO_2NP-0.1/SNM, (B) poly(HID-tma)-0.5/SiO_2NP-0.5/SNM, (C) poly(HID-tma)-0.5/SiO_2NP-2/SNM, and (D) poly(HID-tma)-0.5/SiO_2NP-3/SNM [28].

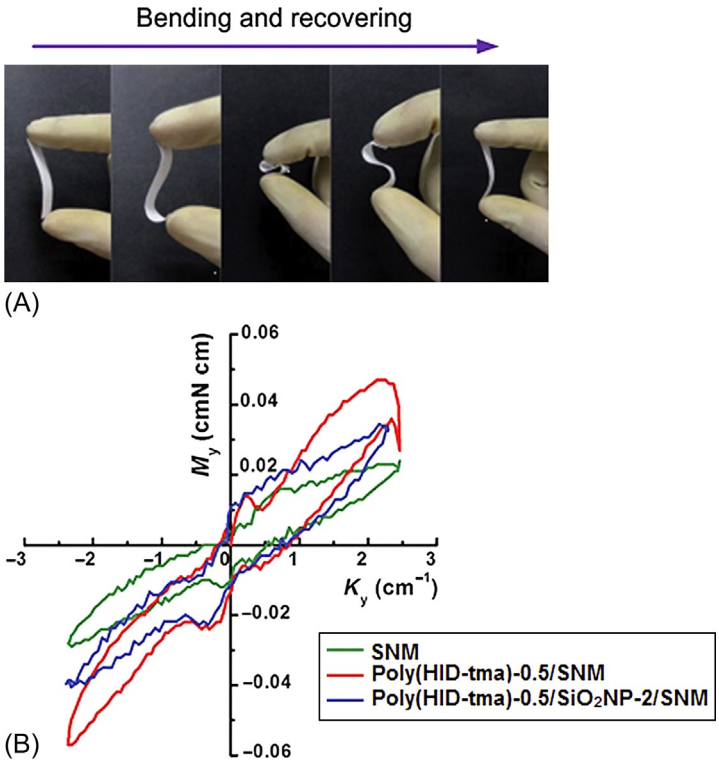

FIG. 3 (A) Optical images presenting the flexibility of poly(HID-tma)-0.5/SiO_2NP-2 by bending and recovering. (B) KES-FB2 test carried out on the relevant SNM, poly(HID-tma)-0.5/SNM, and poly(HID-tma)-0.5/SiO_2NP-2/SNM [28].

and then the stress-strain curves showed a typical linear increase until the yield stress was reached. Meanwhile, the final elongations at break of the modified membranes were greatly decreased, compared to SNM, which could be attributed to the inhibition of fiber slip by poly(HID-tma) layers. The results showed that the poly(HID-tma)/SiO_2NP/SNM possessed good thermal stability, excellent flexibility, and comparable tensile strength, which are of great importance for superhydrophobic membranes that are intended for real applications [64,65]. Therefore these membranes could be applied as promising materials for a wide range of potential applications in high-temperature filtration, self-cleaning coatings, catalyst carriers, and so on.

2.2 Superhydrophobic and Superoleophilic Nanofibrous Membrane by In Situ Polymerization of Benzoxazine for Oil-Water Separation

Tang and coworkers prepared superhydrophobic and superoleophilic nanofibrous membranes by modifying the

high-strength poly(*m*-phenylene isophthalamide) (PMIA) nanofibers with fluorinated polybenzoxazine/SiO_2NPs functional layer (Fig. 4) [28]. A novel bifunctional fluorinated benzoxazine (HID-oda) synthesized from 4,4′-(hexafluoroisopropylidene) diphenol, octadecylamine, and paraformaldehyde was used as the starting monomer for the surface modification of PMIA nanofibrous membranes. Initially, carbon nanotube–reinforced PMIA nanofibrous membranes were produced by electrospinning, and then poly(HID-oda)/SiO_2NP–modified PMIA nanofibrous membranes were fabricated by varying the concentration of HID-oda (0.05, 0.1, 0.5, 1, and 4 wt%) and SiO_2NP (0.1, 0.5, 1, and 2 wt%). First, nanofibrous membranes were dipped into HID-oda solutions. Subsequently, in situ polymerization was achieved upon curing at 200°C, and a cross-linked thermosetting layer (poly(HID-oda)) formed on the fibers' surface. The obtained PMIA membranes modified from the HID-oda concentration of *x* wt% were denoted as poly(HID-oda)-*x*. Similarly, the relevant poly(HID-oda)/SiO_2NP–modified PMIA samples were denoted as poly(HID-oda)-*x*/SiO_2NP-*y*/PMIA, where *x* is the concentration of HID-oda (*x* wt%) and *y* is the concentration of SiO_2NP (*y* wt%).

WCA measurements of poly(HID-oda)/SiO_2NP/PMIA with the low HID-oda concentrations of 0.05, 0.1, 0.5, and 1 wt% showed a remarkable increase in WCAs of 54, 89, 118, and 120 degrees, respectively. On the other hand, further increasing the concentration of HID-oda (>2 wt%) decreased the WCA to about 103 degrees. The incorporation of SiO_2NP in the poly(HID-oda) functional layer significantly changed the morphology of the resulting membranes by the formation of nano-scaled rough structures on the surfaces of nanofibers (Fig. 5).

The WCA of poly(HID-oda)/SiO_2NP/PMIA nanofibrous membranes prepared from 1 wt% HID-oda and 0.1, 0.5, 1, and 2 wt% of SiO_2NP was 120, 137, 148, 155, and 161 degrees, respectively, indicating a remarkable increase of WCA toward the increasing SiO_2NP contents (Fig. 6A). In contrast, the OCA of poly(HID-oda)-1/SiO_2NP-2/PMIA membrane showed inverse behavior with a comparable superoleophilic with an extremely low OCA of 0 degrees, whereas that value is 23 degrees for pristine oleophilic PMIA membranes. Here, again, the introduction of the appropriate roughness with a multiscale range makes the hydrophobic surface more hydrophobic and the oleophilic surface more oleophilic, as suggested by the Wenzel and the Cassie-Baxter models [50,51]. This promising selective wettability makes the membranes good candidates for oil-water separation.

Moreover, hydrophobicity of a poly(HID-oda)-1/SiO_2NP-2/PMIA membrane at high temperatures and in a broad range of pH 2–12 was investigated. This membrane

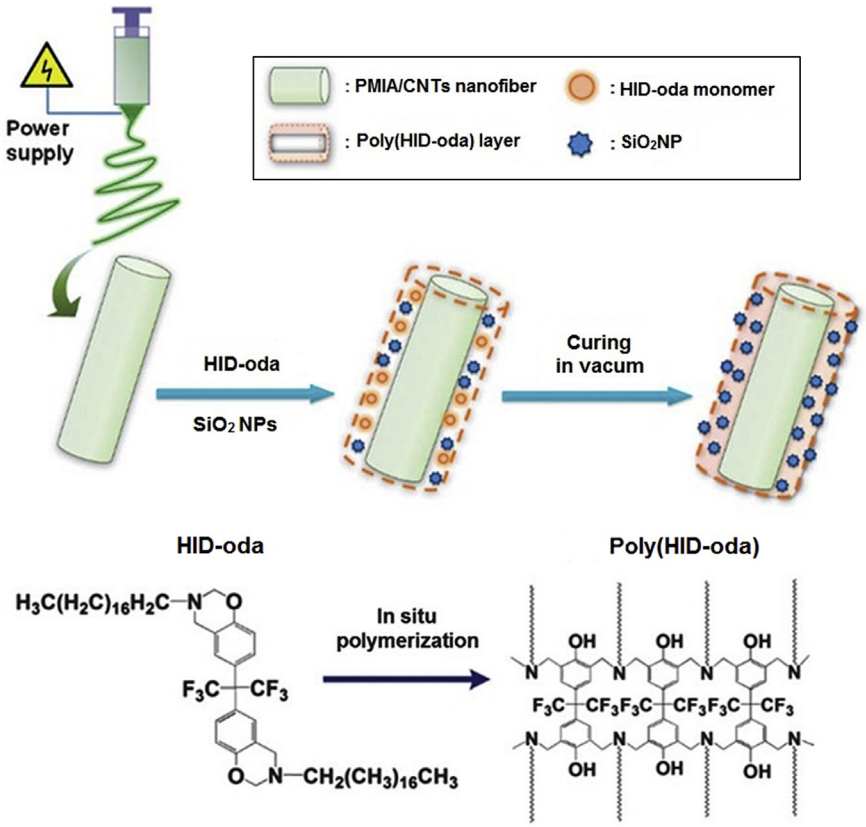

FIG. 4 Illustration showing the synthesis procedure of poly(HID-oda)/SiO_2NP/PMIA nanofibrous membranes and the relevant formation mechanism [29].

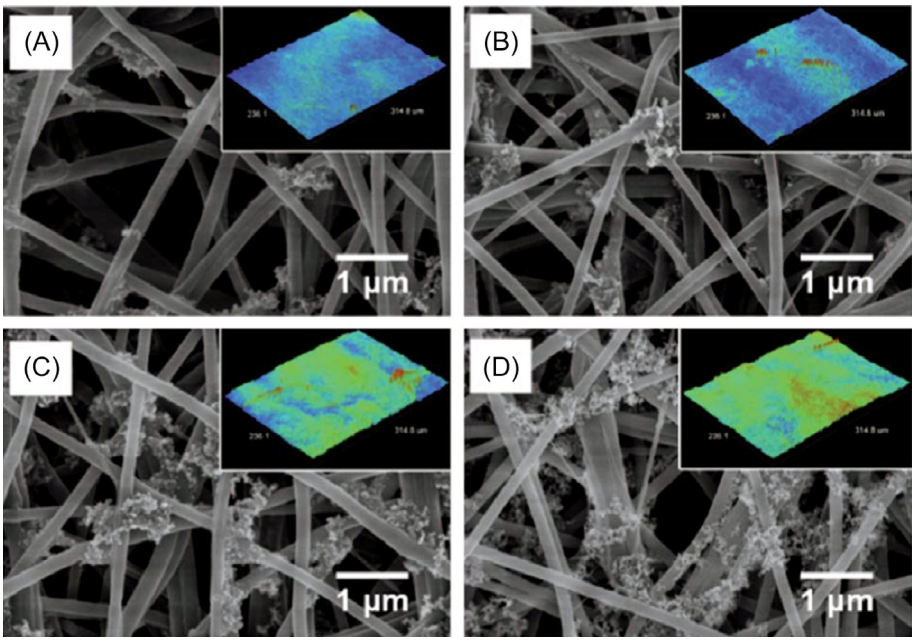

FIG. 5 FE-SEM images of (A) poly(HID-oda)-1/SiO_2NP-0.1/PMIA, (B) poly(HID-oda)-1/SiO_2NP-0.5/PMIA, (C)poly(HID-oda)-1/SiO_2NP-1/PMIA, and (D) poly(HID-oda)-1/SiO_2NP-2/PMIA membranes. The insets show the corresponding optical profilometry images of each sample [29].

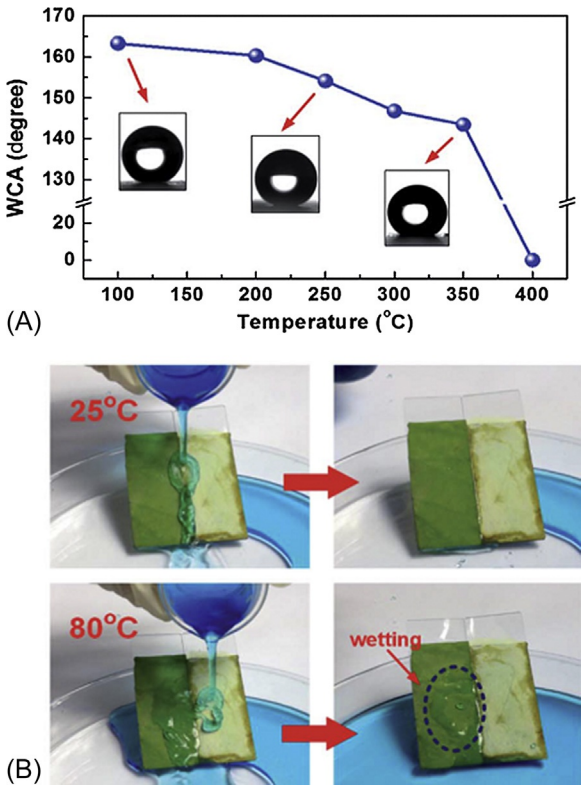

FIG. 6 (A) WCAs and the corresponding shapes of water droplets on the poly(HID-oda)-1/SiO_2NP-2/PMIA membrane after calcination at different temperatures for 10 min. (B) Optical photos of cool water (25°C) and hot water (80°C) dumped on the surface of lotus leaves (left darker one) and the poly(HID-oda)-1/SiO_2NP-2/PMIA membrane (right lighter one), the water was dyed with methyl blue [29].

exhibited superhydrophobicity toward water at all pH values and heat treatments up to 250°C. After a heat treatment at 350°C, the poly(HID-oda)-1/SiO_2NP-2/PMIA membrane maintained promising hydrophobicity with the WCA at 143 degrees. In addition, the repellent characteristics of the poly(HID-oda)-1/SiO_2NP-2/PMIA membrane to hot water was comparable to that of the classic superhydrophobic lotus leaves as well (Fig. 6B). Although both the lotus leaves (left green one) and poly(HID-oda)-1/SiO_2NP-2/PMIA membrane (right yellow one) exhibited good repellency toward water at room temperature, the lotus leaves showed hydrophilic properties toward the water at 80°C, indicating the deterioration of the surface hierarchical rough structure. However, the poly(HID-oda)-1/SiO_2NP-2/PMIA membrane still showed robust hydrophobicity toward hot water without wetting, which was due to the excellent stability of the poly(HID-oda) functional layer.

They also measured the quantitative pore size distribution (PSD) of the surface-modified membranes by employing the Barrett-Joyner-Halenda method. It was observed that all membranes with 1 wt% HID-oda and different SiO_2NP concentrations showed a typical polydisperse porous structure with a primary PSD in the range of 20–60 nm and well-developed peaks centered at 34 nm. Moreover, the pore volumes and surface areas increased greatly with increasing SiO_2NP contents, with the poly(HID-oda)-1/SiO_2NP-2/PMIA membrane possessing the highest pore volume of 0.547 $cm^3\ g^{-1}$ and surface area of 57.9 $m^2\ g^{-1}$. As a proof of concept, a gravity-driven oil-water separation experiment

was performed, and it was observed that the oil quickly passed through the membranes within 3 min without any external force, whereas all of the water was retained above the membranes because of the superhydrophobicity and low water-adhesion of the membranes.

Likewise, Shang and coworkers from the same research group reported the fabrication of superhydrophobic and superoleophilic cellulose acetate (CA) nanofibers by in situ polymerization of the fluorinated benzoxazine incorporating a SiO_2NP functional layer on electrospun nanofibers [30]. Here HID-tma was used as a starting monomer, which could directly form a hydrophobic cross-linked thermosetting polymer (poly(HID-tma)) layer on the nanofiber surface through in situ polymerization. Again, the concentrations of HID-tma (0.01, 0.02, 0.05, 0.1, 1, and 4 wt%) and SiO_2NP (0.1, 0.5, 1, and 2 wt%) were regulated to add promising superhydrophobic and superoleophilic characteristic to the pristine hydrophilic CA nanofibrous membranes. The subsequent curing process was the same as the one used in the preceding study. Similarly, the relevant poly(HID-tma)/SiO_2NP–modified CA samples were denoted as poly(HID-tma)-*x*/SiO_2NP-*y*/CA, where *x* is the concentration HID-tma (*x* wt%), and *y* is the concentration of SiO_2NP (*y* wt%). As is well known, CA is an esterifiable natural polymer containing hydrophilic acetate and hydroxyl groups; therefore, the CA nanofibrous membranes have revealed a superhydrophilic feature with a WCA of less than 5 degrees (Fig. 7A). On the other hand, the WCA of the CA nanofibrous membranes increased significantly after modification with 0.01, 0.02, 0.05, and 0.1 wt% (HID-tma), and corresponding WCAs of 68, 90, 121, and 136 degrees were measured, respectively. Meanwhile, a further increases in concentration have shown a stable tendency toward WCA (Fig. 7A), which demonstrates that the use of a critical concentration of the HID-tma monomer is required to induce the hydrophobicity among the CA nanofibrous membranes.

By the incorporation of 0.1, 0.5, 1, and 2 wt% SiO_2NP into the 1 wt% HID-tma, nano-scale hierarchical structures were formed on the fiber surfaces, which enhanced the surface roughness. Because rough surfaces retain less contact with water droplets, a considerable increase was observed in the WCA of poly(HID-tma)/SiO_2NP–modified CA nanofibrous membranes, and the corresponding WCAs of the membranes were measured at 120, 137, 148, 155, and 161 degrees, respectively. In contrast, OCA of membranes have shown a reverse tendency, and the OCA of the FCA-1/SNP-2 membrane was extremely low (3 degrees) when compared to the pristine oleophilic CA membranes (25 degrees).

Moreover, the hierarchical rough structure analysis revealed the majority of mesopores in membranes since a series of typical adsorption behaviors, including monolayer adsorption, multilayer adsorption, and capillary condensation, could be observed (Fig. 8A). Also a Brunauer-Emmett-Teller (BET) surface area analysis of poly(HID-tma)-1/SiO_2NP/CA

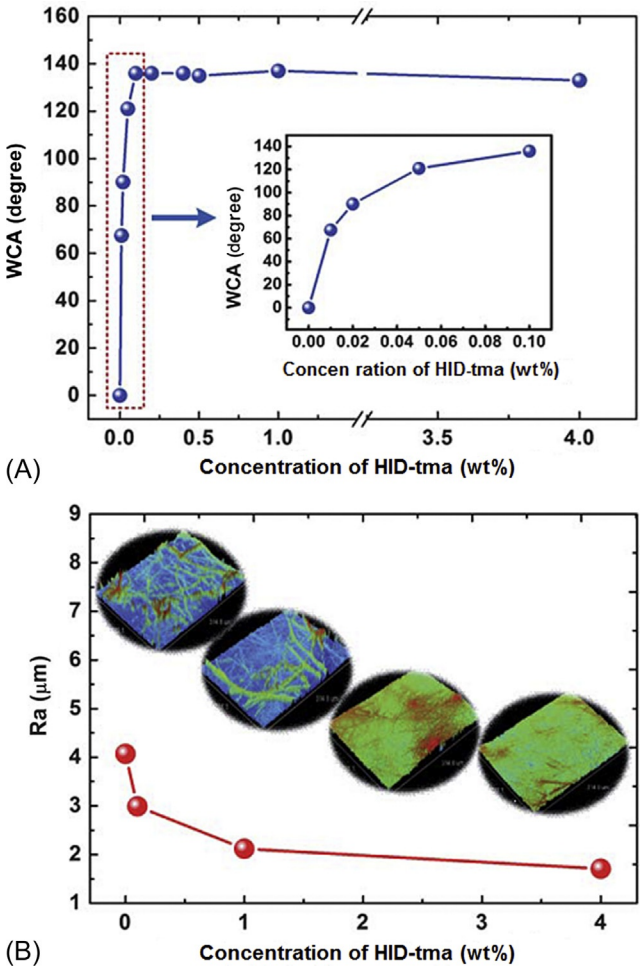

FIG. 7 (A) WCAs of the various modified CA nanofibrous membranes with different concentrations of HID-tma. (B) The Ra values of selected CA, poly(HID-tma)-0.1/CA, poly(HID-tma)-1/CA, and poly(HID-tma)-4/CA nanofibrous membranes (the insets are the corresponding optical profilometry images) [30].

membranes revealed a considerable increase of the surface area that was caused by the increasing SiO_2NP contents in the poly (HID-tma) medium, and the highest surface area was observed for the poly(HID-tma)-1/SiO_2NP-2/CA nanofibrous membranes at 59.0 $m^2\ g^{-1}$, indicating the major contributing role of SiO_2NP. PSD analysis showed that the poly(HID-tma)-1/SiO_2NP/CA membranes possess a typically polydisperse porous structure and a primary PSD in the range 20–60 nm, and a relatively concentrated PSD mainly centered at 40 nm was observed in all samples (Fig. 8B). Moreover, the values of these peaks greatly increased along with the increasing SiO_2NP contents, indicating the remarkable enhancement of the mesoporous structure.

Poly(HID-tma)-1/SiO_2NP-2/CA membranes were prepared in a large scale (60 × 60 cm) with a thickness of 50 mm (Fig. 9A) because of their great versatility in scaling up production. In addition, poly(HID-tma)-1/SiO_2NP-2/CA membranes revealed similar superhydrophobic behavior

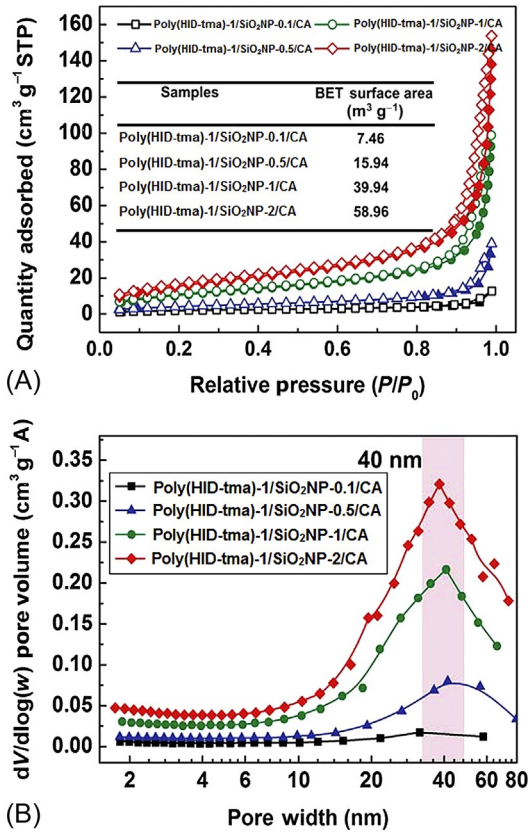

FIG. 8 (A) N_2 adsorption-desorption isotherms of relevant poly(HID-tma)-1/SiO_2NP-0.1/CA, poly(HID-tma)-1/SiO_2NP-0.5/CA, poly(HID-tma)-1/SiO_2NP-1/CA, and poly(HID-tma)-1/SiO_2NP-2/CA membranes. (B) Pore distribution of relevant membranes using the Barrett-Joyner-Halenda method [30].

toward water with different pH measurements, exhibiting the excellent stability and usability (Fig. 9B) [66–68]. Besides, since these membranes possess selective wettability and high porosity, they demonstrated effective performance for separation of oil-water mixtures in a very short time (30 s) as shown in Fig. 9C.

3 POLYBENZOXAZINE/POLYMER COMPOSITE NANOFIBERS

3.1 Low-Surface-Free-Energy Polybenzoxazine/PAN Fibers for Non-Biofouling Membrane

Kao and coworkers demonstrated a facile fabrication of nonfluorine and nonsilicon low-surface-free-energy fibers from the electrospinning of PAN and a phenol-aniline–based benzoxazine (P-a) blend solution [69]. Generally, it is difficult to obtain nanofibers from monomers or small molecules because chain entanglement and overlapping are the key factors for the formation of nanofibers during the electrospinning process. Therefore PAN, which is an ideal blend material because of its high melting temperature [22] and good miscibility with the P-a monomer, was used as the carrier matrix, and it was aimed at improving the practical application of polybenzoxazine as superhydrophobic fibrous mats. The total concentration of PAN and P-a was maintained at 10% in the solution, and the PAN:P-a weight fractions (100:0, 70:30, 50:50, 30:70, and 0:100) were varied to produce PAN/P-a hybrid fibers by electrospinning. Nanofibers obtained from these compositions were denoted as PAN10/P-a0, PAN7/P-a3, PAN5/P-a5, PAN3/P-a7, and PAN0/P-a10, respectively. The miscibility and curing behavior of the hybrids along with the typical P-a were examined by means of differential scanning calorimetry (DSC). For a hybrid of macromolecules, a single peak detected by DSC is conventionally employed as a criterion reflecting the miscibility of the hybrid. The results exhibit that the significant miscibility of the PAN/P-a hybrids occurred below 50 wt% P-a in the PAN, indicating that P-a could be dissolved completely in the PAN phase with a 50 wt% concentration. However, two peaks appeared at c.200°C and 250°C for PAN3/P-a7, indicating the occurrence of the phase separation at 70 wt% P-a content (Fig. 10).

Thermally activated ring-opening and cross-linking of P-a yield the poly(P-a) networks, which have many phenolic hydroxyl groups. In addition, PAN is stabilized by heating in air at temperatures in the range of 200–300°C. These phenolic hydroxyl groups of poly(P-a) interact through hydrogen bonding with the heteroaromatic or polyimine cyclic structure that occurs during the stabilization of PAN, which can be readily investigated by means of Fourier transform infrared spectroscopy (FTIR) (Fig. 11). Three different kinds of OH groups and two different kinds of NH groups are present in the PAN/poly(P-a) mixtures. The broad band in the range of 3200–3600 cm^{-1} increased, verified that the intermolecular hydrogen bonding between PAN and poly(P-a) occurred. The area of the broad band of the PAN5/poly(P-a)5 blend approaches a maximum, indicated that the strongest intermolecular hydrogen bonding between PAN and poly(P-a) occurred at the 50 wt% concentration P-a blending with PAN. These results indicated that the intramolecular hydrogen bonding of poly(P-a) transferred substantially to intermolecular hydrogen bonding with PAN.

The increase in the concentration of the P-a in the PAN solution had a considerable effect on the fiber diameter and morphology. Fiber diameters of the PAN/P-a hybrid and PAN/poly(P-a) blend fibers are summarized in Table 1. The static water contact angle (SWCA) of the PAN/P-a and PAN/poly(P-a) nanofibers and spin-coated PAN/P-a and PAN/poly(P-a) hybrid surfaces were also investigated. The cured PAN5/poly(P-a)5 nanofibers possessed the highest SWCA of 154 ± 2 degrees, indicating the superhydrophobicity of surfaces. If the air fraction is high enough, a very hydrophobic surface is realized. For the PAN/P-a hybrid surface, the air fraction was calculated to be in the

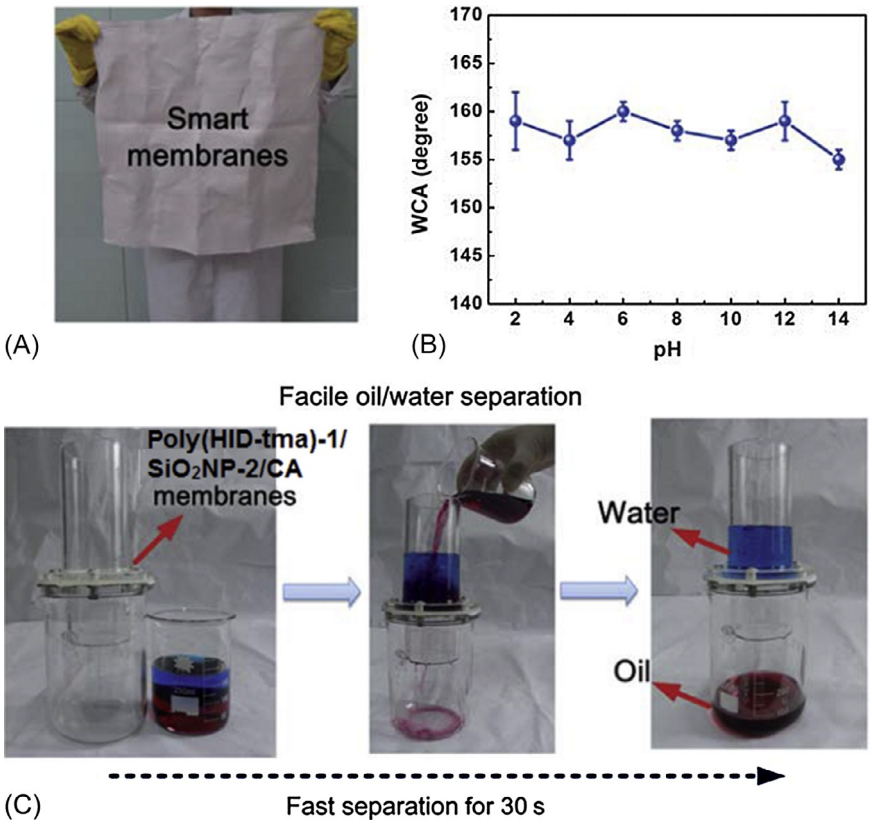

FIG. 9 (A) Photograph shows the large scale (60 × 60 cm) of poly(HID-tma)-1/SiO_2NP-2/CA membranes. (B) The relationship between pH and the WCAs of poly(HID-tma)-1/SiO_2NP-2/CA membranes. (C) The facile oil-water separation using poly(HID-tma)-1/SiO_2NP-2/CA membranes; the water and oil were dyed by methyl blue and red, respectively [30].

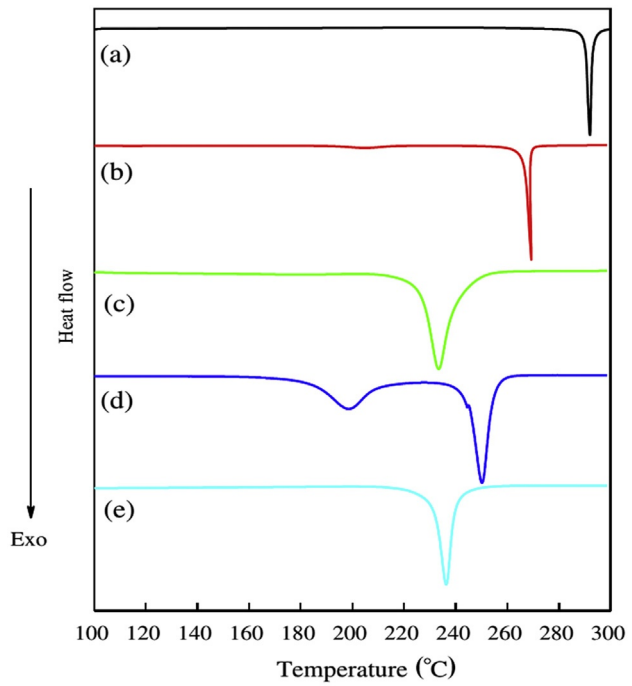

FIG. 10 Conventional first run DSC thermograms of the PAN/BA hybrids including (a) PAN10/poly(P-a)0, (b) PAN7/poly(P-a)3, (c) PAN5/poly(P-a)5, (d) PAN3/poly(P-a)7, and (e) PAN0/poly(P-a)10, respectively.

range of 0.524–0.63 upon 50 wt% of P-a content (Table 1). The thermal treatment process collapsed the hybrid fiber layer slightly, but raised all air fractions of the fibrous mats. From the SWCAs on the PAN5/poly(P-a)5 surface, the air fraction was calculated to be 0.86, indicating that about 86% of the PAN/poly(P-a) surface was occupied by air. Therefore hydrophobicity of the fibrous mats was believed to be mainly caused by the trapped air between the fibers, and the poly(P-a) content in the fibers. The sliding behavior of a water droplet is mainly related to contact angle hysteresis, which is defined as the difference between advancing and receding contact angles, and to the continuity of a three-phase (solid-liquid-air) contact line [34]. Contact angle hysteresis of all nanofibers are summarized in Table 2. The packed fibrous structure of the PAN5/poly(P-a)5 surface was the key contributor to the enhancement of hydrogen bonds, gave high adhesion between water and the low-surface-energy mat [38]. As shown in Fig. 12, all four number ratios of PAN/poly(P-a) fibers, such as PAN10/poly(P-a)0, PAN7/poly(P-a)3, PAN5/poly(P-a)5, and PAN3/poly(P-a)7, also had the high adhesion forces of fibrous mats, even when the surfaces were tilted. Therefore the high adhesion properties of the PAN/poly(P-a) fibrous mats for water resulted from hydrogen bonding caused by the OH group of PAN/poly(P-a) fibrous mats.

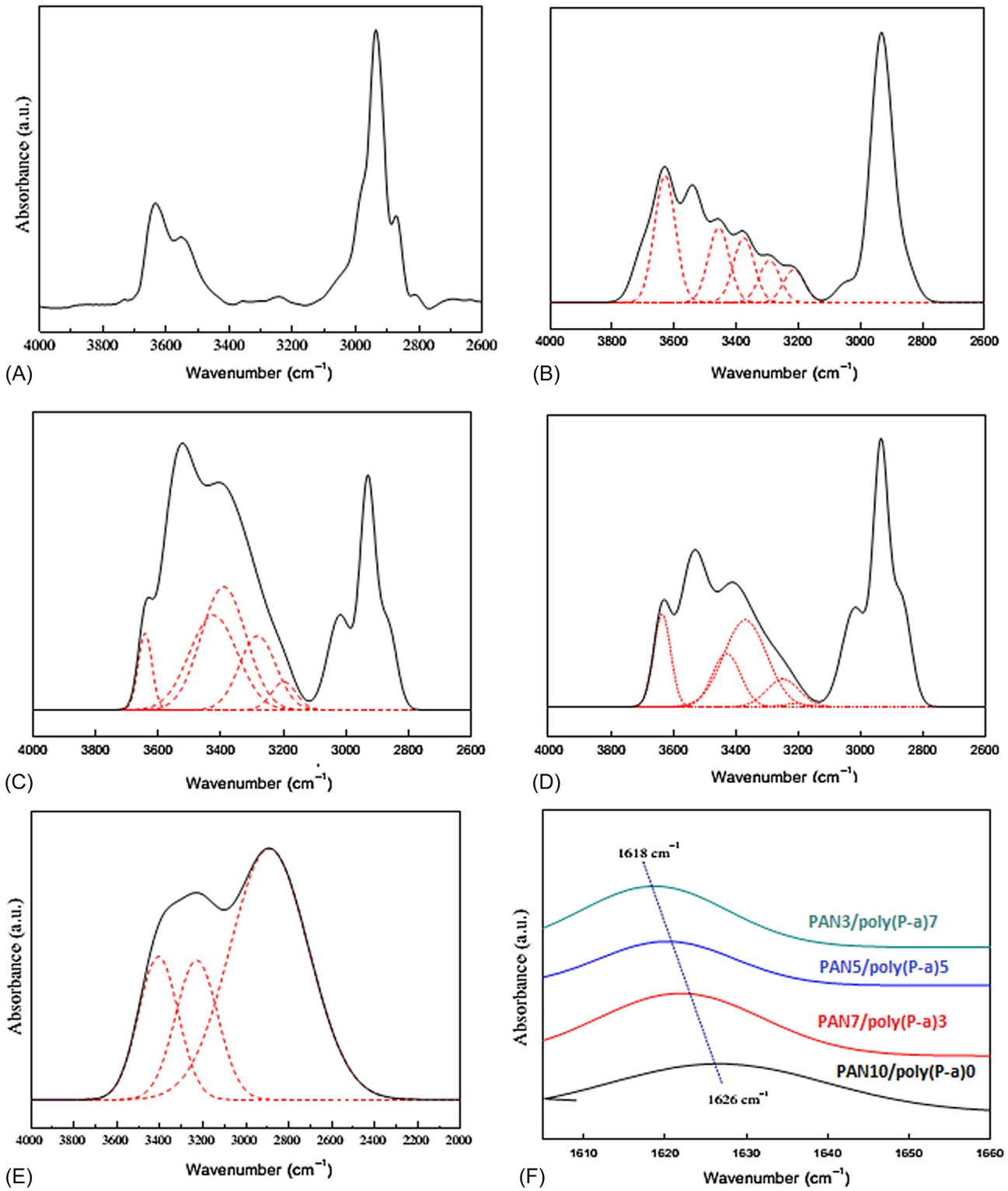

FIG. 11 Expanded FTIR spectra in the range of 4000–2000 cm^{-1} for (A) PAN10/poly(P-a)0, (B) PAN7/poly(P-a)3, (C) PAN5/poly(P-a)5, (D) PAN3/poly(P-a)7, (E) PAN0/poly(P-a)10 with corresponding curve fitting, and (F) at the C–N stretching band region of PAN/poly(P-a) blends for PAN10/poly(P-a)0, PAN7/poly(P-a)3, PAN5/poly(P-a)5, and PAN3/poly(P-a)7 at room temperature.

TABLE 1 Fiber Diameter, SWCAs, Hysteresis, and Fractional Interfacial Areas of Solid and Air Contact With a Water Droplet (f_1 and f_2) for PAN/Poly(P-a) Hybrids and PAN/Poly(P-a) Blend Fiber Mats Prepared by Electrospinning and Spin-Coating, Respectively [70]

Samples	Fiber Diameter (nm)	SWCA		Hysteresis[a]		Fractions of a Fiber's Contact With a Water Droplet (f_1)[b]	Fractions of Air Contact With a Water Droplet (f_2)[b]
		Spin-Coating (Degrees)	Electrospinning (Degrees)	Spin-Coating (Degrees)	Electrospinning (Degrees)		
PAN10/P-a0	456 ± 97.2	44 ± 3	100.5 ± 3	6	16	0.475	0.524
PAN7/P-a3	478 ± 152.3	55.8 ± 3	110 ± 2	11	40	0.421	0.578
PAN5/P-a5	494 ± 72.7	69.4 ± 2	120 ± 2	11	34	0.369	0.63
PAN3/P-a7	1144 ± 173.1	83.5 ± 3	104 ± 3	12	2	0.68	0.31
PAN10/poly(P-a)0	430 ± 95.2	49 ± 3	108.3 ± 3	15	31	0.291	0.709
PAN7/poly(P-a)3	466 ± 77.9	68.2 ± 3	120 ± 2	19	20	0.261	0.738
PAN5/poly(P-a)5	482 ± 74.0	88.3 ± 2	154 ± 2	18	16	0.13	0.86
PAN3/poly(P-a)7	1130 ± 280.9	93.2 ± 3	112 ± 3	22	1	0.663	0.336

[a] *Difference between advancing and receding contact angles.*
[b] *Calculated by equations 1* $\cos\theta_r = r\cos\theta_s$ *and* $\cos\theta_r = f_1\cos\theta_s - f_2$*; where* θ_r *and* θ_s *are the equilibrium (Young's) SWCA of a rough surface and a smooth surface, respectively.* f_1 *and* f_2 *are the fractions of a solid surface and air in contact with a liquid droplet, respectively* ($f_1 + f_2 = 1$).

Fluorescein isothiocyanate (FITC) is a derivative of fluorescein used in wide-ranging applications including flow cytometry.

Here, Kao and coworkers used FITC-conjugated antibodies as the probe proteins to evaluate their effects on the non-biofouling performance of the prepared fibers. It was found that the original PAN fibers were also highly susceptible to protein adsorption. In comparison to the PAN/P-a hybrid fibers, note that the amount of antibodies on the PAN/poly (P-a) blend fiber surfaces apparently decreased when the poly(P-a) content increased to 50 wt%. Most of the FITC-conjugated antibodies adhered solely to the fibers with a diameter in the range of 3–5 μm for PAN7/poly(P-a)3 and PAN5/poly(P-a)5 because of their larger contact area with the antibodies. Most of the blend fibers with a diameter below 500 nm exhibited an excellent non-biofouling performance. The laser scanning confocal microscope (LSCM) studies clearly demonstrate that blending sufficient poly(P-a) with PAN can significantly change the surface-free-energy of fibers, and thus improve the protein adsorption resistance.

4 POLYBENZOXAZINE-BASED MCNFs

4.1 Synthesis of Mesoporous Magnetic Fe_3O_4@Carbon Nanofibers Utilizing In Situ Polymerized Polybenzoxazine for Water Purification

Si et al. first reported the successful production of polybenzoxazine–based MCNFs with enhanced mesoporous structures and excellent adsorption performance by combining the electrospinning and an in situ polymerization approach [72]. First, composite nanofibers (PVBNFs) were

TABLE 2 Structure Parameters of Hierarchical Porous Fe_3O_4@CNFs [71]

Samples	Primary Structures				Secondary Structures			
	SSA[a] ($m^2\ g^{-1}$)	TPV[b] ($cm^3\ g^{-1}$)	V_{micro}[c] ($cm^3\ g^{-1}$)	V_{meso}[d] ($cm^3\ g^{-1}$)	PVF_{meso}[e] (%)	D_1[f]	D_2[g]	D_1/D_2
Fe@CNF-1	513	0.617	0.104	0.513	83.1	2.45±0.02	2.67±0.01	0.917
Fe@CNF-2	405	0.510	0.101	0.409	80.2	2.51±0.01	2.73±0.01	0.919
Fe@CNF-3	629	0.911	0.101	0.810	88.9	2.32±0.02	2.46±0.01	0.943
A-Fe@CNF-1	1037	1.03	0.273	0.755	73.4	2.54±0.01	2.70±0.02	0.941
A-Fe@CNF-2	1207	1.43	0.074	1.36	94.8	2.28±0.02	2.47±0.01	0.923
A-Fe@CNF-3	1885	2.30	0.183	2.12	92.1	2.30±0.02	2.54±0.02	0.906

[a]*Specific surface area (SSA) was calculated by the BET method.*
[b]*Total pore volume (TPV) (<25 nm) was estimated using 2D-NLDFT method.*
[c]V_{micro} *is the micropore (<1.7 nm) volume calculated by the Horvath-Kawazoe (HK) method.*
[d]V_{meso} *was obtained based on the TPV and* V_{micro} *values.*
[e]PVF_{meso} *indicates the pore volume fraction of mesopores.*
[f]D_1 *indicates the surface fractal dimension determined from the* N_2 *adsorption analysis method.*
[g]D_2 *was the surface fractal dimension calculated from small-angle X-ray scattering (SAXS) measurements.*

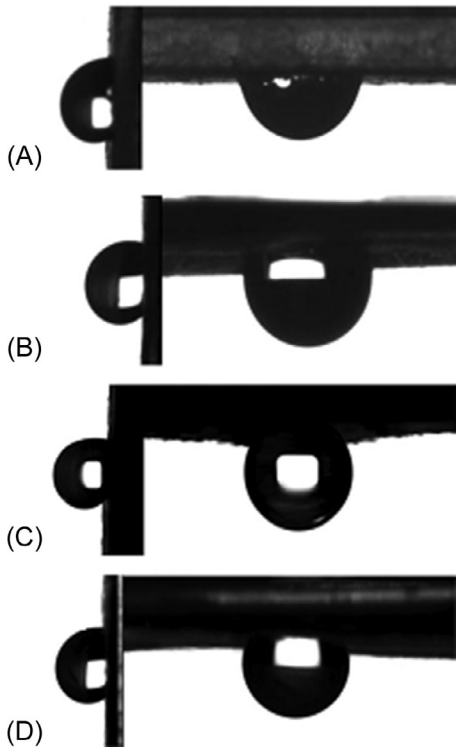

FIG. 12 Shapes of a water droplet on the electrospun PAN/poly(P-a) hybrid fiber surface with different tilt angles: 90 *(left)* and 180 *(right)* for (A) PAN10/poly(P-a)0, (B) PAN7/poly(P-a)3, (C) PAN5/poly(P-a)5, and (D) PAN3/poly(P-a)7, respectively [69].

obtained from a polyvinylbutyral (PVB), bisphenol-A-aniline–based benzoxazine (BA-a), and ferric acetylacetonate ($Fe(acac)_3$) mixture solution, followed by in situ polymerization of BA-a at 230°C performed in vacuum. During this process, PVB fiber bulk decomposed gradually, and BA-a monomers polymerized into poly(BA-a) by ring-opening reactions and cross-linking. As a result, poly(BA-a) nanofibers (poly(BA-a)NFs) were obtained as original fiber morphology. This utilized the properties of near-zero shrinkage and no generation of by-products from the polymerization of benzoxazines [42]. Finally, poly(BA-a) NFs were activated (A-poly (BA-a)NFs) by using KOH solution and then carbonized at 850°C to obtain the activated Fe_3O_4@carbon nanofibers (A-Fe@CNFs) (Fig. 13). The obtained nanofibers randomly produced bended morphology with an average fiber diameter of 110 nm and a porous graphitic structure embedding Fe_3O_4 nanocrystals with a grain-size range of 10–20 nm (Fig. 14).

Unactivated samples (Fe@CNFs) were also prepared for comparison, and it was observed that the surface area and pore volume of Fe@CNFs (629 $m^2\ g^{-1}$ and 0.921 $cm^3\ g^{-1}$) greatly increased after activation (A-Fe@CNFs, 1885 $m^2\ g^{-1}$ and 2.325 $cm^3\ g^{-1}$), which is higher than that of conventional PAN–based CNFs. Also, microporous and mesoporous structures of both nanofibers were investigated and results showed that, according to microporous analysis, the cumulative pore volume (pore size 0.5–1.2 nm) increased from 0.1 to 0.18 $cm^3\ g^{-1}$ by activation and that, according to mesoporous analysis, the A-Fe@CNFs (2.083 $cm^3\ g^{-1}$) showed a remarkable increase of cumulative pore volume (pore size 1.8–55.7 nm) over that of

Fe@CNFs (0.874 cm^3 g^{-1}). It can be inferred that the KOH activation mostly enhanced the mesoporous structure of fibers and that it is the main reason for the significant increase in surface area. In addition, the adsorption performance of as-prepared magnetic mesoporous A-Fe@CNF was investigated with methylene blue (MB) and rhodamine B (RhB) dyes, and complete adsorption was achieved in 10 and 15 min for MB and RhB, respectively. After the adsorption, the aqueous suspension could be separated easily by an external magnet, without the use of a difficult separation procedure, which is of great importance for real applications.

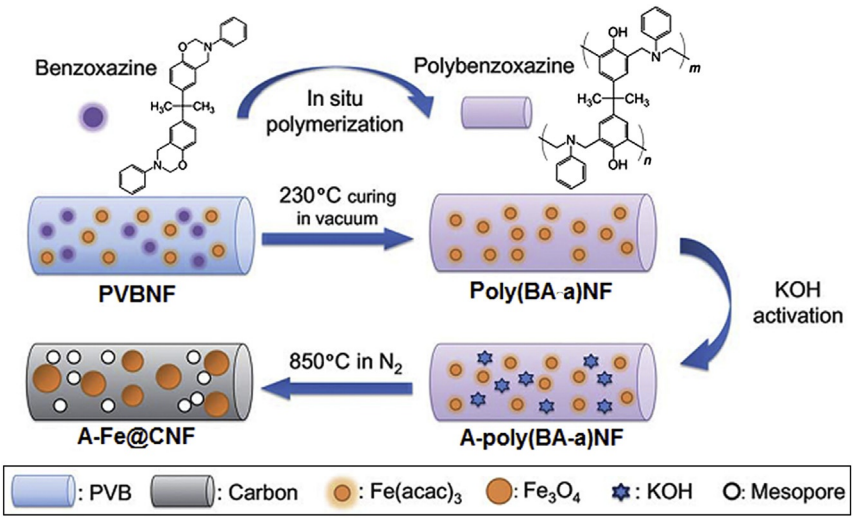

FIG. 13 Schematic for the strategy using the in situ polymerization approach to synthesize A-Fe@CNFs. During carbonization, poly(BA-a) NF and $Fe(acac)_3$ gradually converted to carbon nanofibers and Fe_3O_4 nanocrystals, respectively, H_2 and H_2O gases from the decomposition of KOH yielded pores in the carbon nanofibers [72].

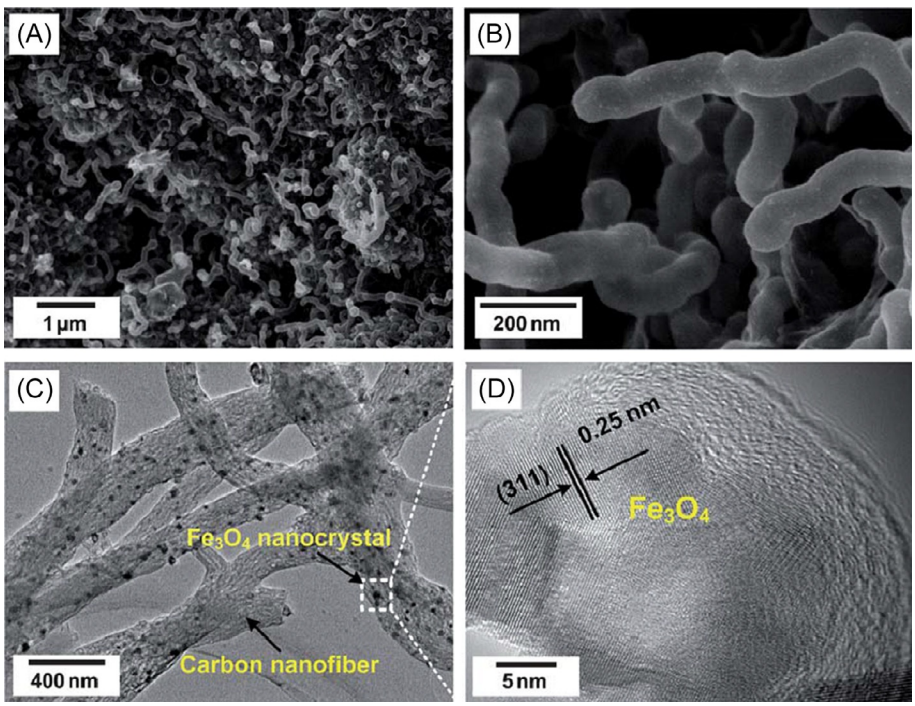

FIG. 14 (A) Low and (B) high magnification FE-SEM images of A-Fe@CNFs; (C) TEM image of A-Fe@CNFs; (D) HRTEM image showing Fe_3O_4 nanocrystals in (311) orientation embedded in carbon nanofibers [72].

4.2 Fabrication of Magnetic Polybenzoxazine–Based CNFs With Fe_3O_4 Inclusions With a Hierarchical Porous Structure for Water Treatment

Si and coworkers produced hierarchical porous, magnetic Fe_3O_4@carbon nanofibers (Fe_3O_4@CNFs) based on polybenzoxazine precursors [70] by using a procedure similar to the preceding one. Here three different compositions of BA-a and PVB were prepared as keeping the total concentration 10 wt%, and the weight ratios of BA-a/PVB were adjusted to 1:3, 1:1, and 3:1 in these compositions. In all samples, the weight ratio of BA-a/$Fe(acac)_3$ was fixed at 4:1 to ensure that the final MCNFs had the identical Fe_3O_4 mass fraction. The obtained solutions were electrospun, and the hybrid nanofibers were produced and denoted as PVBNF-1, PVBNF-2, and PVBNF-3 with the BA-a/PVB weight ratios of 1:3, 1:1, and 3:1, respectively. All PVBNF membranes were polymerized by ring-opening reactions carried out at 250°C under vacuum to get thermosetting poly(BA-a)NF. Subsequently, activation and carbonization procedures were performed as previously done, and A-Fe@CNFs were obtained (Fig. 15). In addition, the unactivated Fe@CNF was prepared for comparison. The poly(BA-a)NF, A-Fe@CNF, and Fe@CNF samples resulting from corresponding PVBNF-x ($x=1$, 2, 3) are referred to as poly(BA-a)NF-x, A-Fe@CNF-x, and Fe@CNF-x ($x=1$, 2, 3), respectively.

The average fiber diameter of corresponding PVBNF-1, PVBNF-2, and PVBNF-3 were 796, 637, and 583 nm, respectively, which showed that the fiber diameter decreased regularly when the BA-a mass fraction increased (Fig. 16A–C). Upon the in situ polymerization at 250°C, the corresponding poly(BA-a) nanofibers (poly(BA-a)NF) obtained from a variety of PVBNFs possessed similar stuck morphology and an average fiber diameter of about 660 nm (Fig. 16D–F). However, after activation and carbonization procedures, the structure and morphology of A-Fe@CNF significantly changed, compared to the original poly(BA-a)NF. The A-Fe@CNF-1 and A-Fe@CNF-2 exhibited typical cataclastic nanorod morphology with small aspect ratios. On the other hand, the A-Fe@CNF-3 preserved the randomly oriented nanofiber morphology with a bended structure and a uniform smooth surface, presumably because of the highly compact cross-linking structure obtained in poly(BA-a)NF with high BA-a content (Fig. 17A–C). Fe_3O_4 nanocrystals with a grain size range of 10–20 nm incorporated in porous CNFs were clearly observed in the transmission electron microscopy (TEM) image of a single nanofiber (Fig. 17D). Moreover, a high-resolution TEM (HRTEM) image demonstrates the well-resolved lattice fringes with an interplane distance of 0.255 nm derived from the (3 1 1) plane of Fe_3O_4 (Fig. 17E).

Comprehensive investigation of the hierarchical porous structure was carried out quantitatively by PSD analysis, and a polydisperse mesoporous structure mainly within a 2–8 nm range was observed. After activation and carbonization, significant enhancement was observed in the mesoporous structures. The detailed analysis results of surface area and pore volume for corresponding samples are summarized in Table 2. It is obvious that the mesopore volume fractions for all samples were higher than 70%, confirming that the majority of pore structures are mesopores in nanofibers. Moreover, the surface area and pore volume

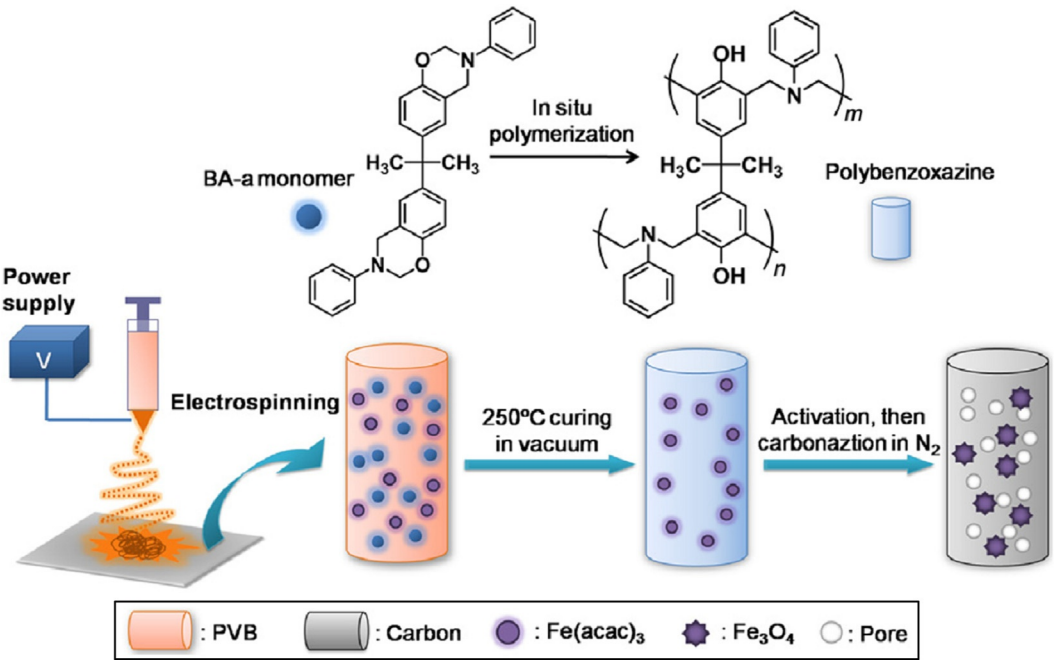

FIG. 15 Illustration showing the synthesis of A-Fe@CNF by a combination of electrospinning and in situ polymerization [70].

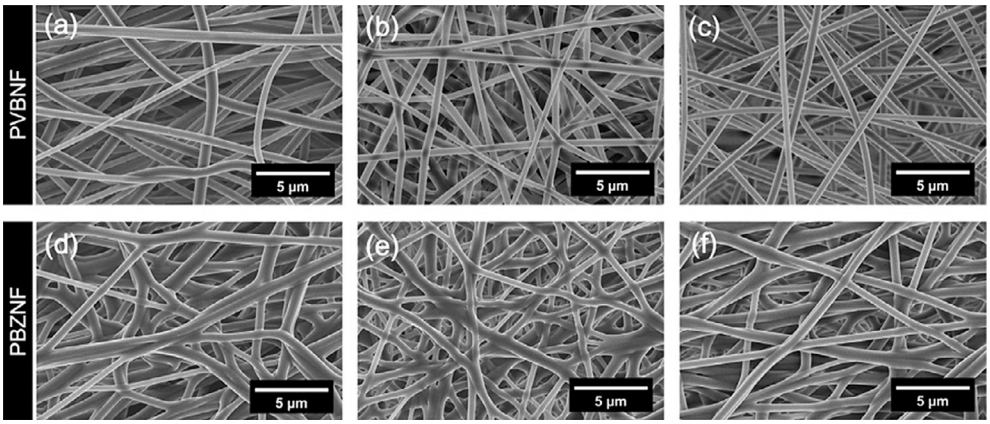

FIG. 16 FE-SEM images of as-spun (A) PVBNF-1, (B) PVBNF-2, and (C) PVBNF-3 and the corresponding cured (D) poly(BA-a)NF-1, (E) poly(BA-a) NF-2, and (F) poly(BA-a)NF-3 [70].

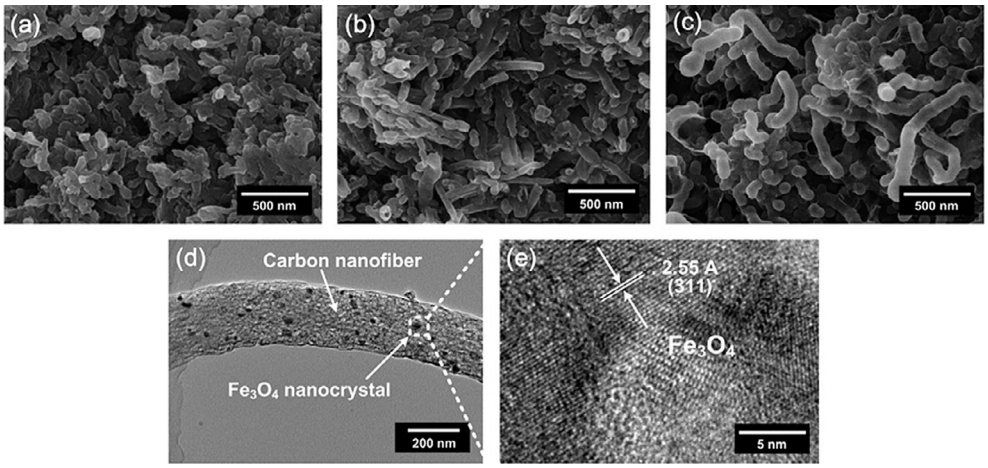

FIG. 17 FE-SEM images of (A) A-Fe@CNF-1, (B) A-Fe@CNF-2, and (C) A-Fe@CNF-3; (D) TEM image of A-Fe@CNF-3; and (E) HRTEM image showing Fe_3O_4 nanocrystals in (311) orientation embedded in MCNFs (A-Fe@CNF-3) [70].

increased with the increase of the BA-a content, as listed in Table 1. Among all samples, A-Fe@CNF-3 possessed a remarkably high surface area of 1885 m^2/g and a pore volume of 2.3 $cm^3\ g^{-1}$.

As in the previous study, the adsorption performance of as-prepared A-Fe@CNF were also tested with MB and RhB dyes. It was found that the A-Fe@CNF-3 possessed the highest adsorption performance achieving complete adsorption of MB and RhB for 10 and 15 min, respectively, and that all samples could achieve complete adsorption of MB and RhB within 15 and 25 min, respectively (Fig. 18).

4.3 PAN/Polybenzoxazine–Based Fe_3O_4@Carbon Nanofibers: Hierarchical Porous Structure and Magnetic Adsorption Property

Tao and coworkers produced a series of magnetic PAN/poly (BA-a)–based Fe_3O_4@CNFs with a tunable morphology and hierarchical porous structure through the combination of a precursor design and an activation process (Fig. 19) [73]. They prepared the precursor solutions by keeping the total concentration of the BA-a and PAN at 12.5 wt% and the amount of $Fe(acac)_3$ fixed at 2 wt% in composite solutions in order to obtain same fraction of Fe_3O_4 in the final MCNFs. The mass fraction of BA-a in the electrospinning solutions was adjusted to 2.5, 5, and 7.5 wt%, and the nanofibers obtained from these three different solutions are denoted as PAN/BA-aNF-1, PAN/BA-aNF-2, and PAN/BA-aNF-3, respectively. Hybrid nanofibers composed of PAN, $Fe(acac)_3$, and different amounts of BA-a were deposited randomly as 3D structures in the form of nonwoven mats. The average fiber diameters of the corresponding PAN/BA-aNF-1, PAN/BA-aNF-2, and PAN/BA-aNF-3 were 486, 322, and 185 nm, respectively, indicating that the fiber diameter decreased steadily with the increase of BA-a content. Initially, the as-spun hybrid nanofibers were heated at 170°C (20 min), 210°C (30 min), and 250°C (60 min) to obtain stabilized thermoset PAN/poly(BA-a) composite

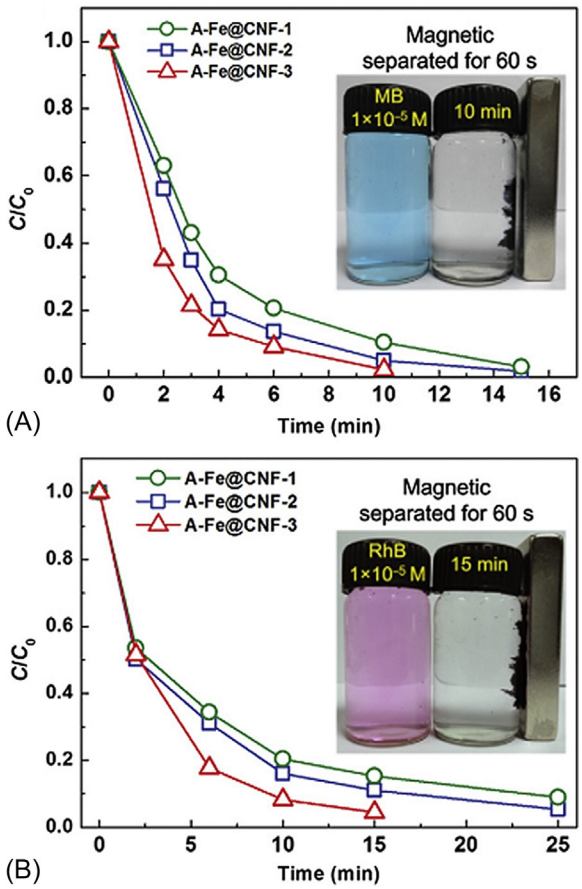

FIG. 18 The C/C_0 versus time plots for adsorption of (A) MB and (B) RhB dye solution. The insets show the magnetic responsive performance (60 s) of A-Fe@CNF-3 after adsorption of MB (10 min) and RhB (15 min) [70].

nanofibers (PAN/poly(BA-a)NF). In this process, the preoxidation of PAN and the in situ polymerization of BA-a occurred at the same time, yielding a thermoset PAN/poly (BA-a)NF precursor. Interestingly, contrary to PAN/BA-aNF samples, the fiber diameter of PAN/poly(BA-a)NF increased significantly with the increase of BA-a, and the average fiber diameters of SNF-1, SNF-2, and SNF-3 were 287, 496, and 732 nm, respectively. In addition, the fibers became stickier with increasing BA-a fraction, which may be explained by the melting behavior of BA-a in a narrow melting range (110–130°C) before being polymerized to a stabilized cross-linked structure [71]. At a higher BA-a fraction, adjacent fibers fuse together because of the strong melting behavior of BA-a upon heat treatment, resulting a sticking fiber with a larger fiber diameter.

The obtained SNF was activated by immersion in the KOH aqueous solution (30 wt%) for 1 h and then dried at 60°C under vacuum. Finally, the activated SNF membranes were carbonized at 850°C for 30 min with a heating rate of 2°C min^{-1} under N_2 flow. During this process, PAN/poly (BA-a) composite nanofibers gradually converted to graphitic nanofibers, and pores formed in fiber bulk because of the released CO and H_2O gases from the decomposition of KOH. Additionally, the embedded Fe_3O_4 nanocrystals were obtained from the thermal decomposition (Td) of $Fe(acac)_3$ during the carbonization process, which could be explained with the burst nucleation and the crystal growth mechanism. After carbonization, the products were washed with 0.1 M HCl, and the black activated Fe_3O_4@CNFs (A-Fe@CNF) was obtained. In addition, the nonactivated Fe_3O_4@CNFs (Fe@CNF) was also prepared for comparison. The SNF, A-Fe@CNF, and Fe@CNF samples prepared from

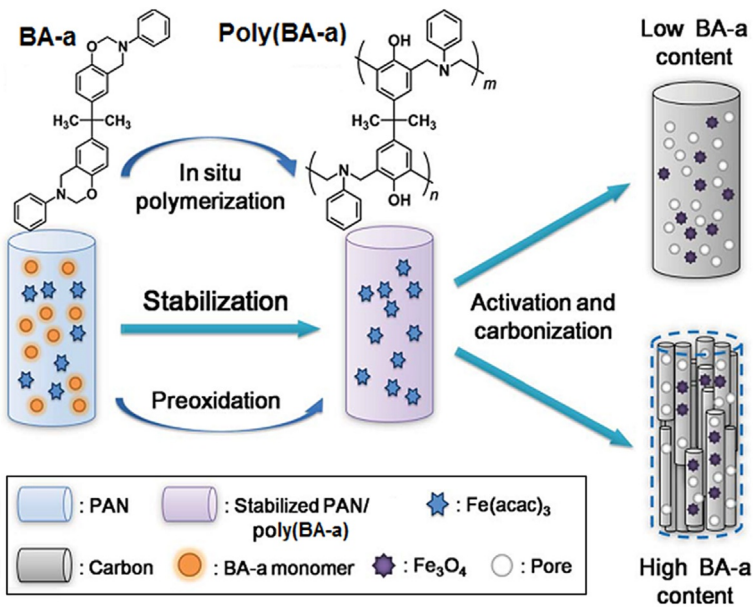

FIG. 19 Synthesis procedures of A-Fe@CNF and the relevant formation mechanisms [73].

corresponding NF-x ($x=1$, 2, 3) are denoted as SNF-x, A-Fe@CNF-x, and Fe@CNF-x ($x=1$, 2, 3).

The structure and morphology of carbonized nanofibers greatly depended on the content of BA-a in precursor fibers. The A-Fe@CNF-1 and A-Fe@CNF-2 showed typical randomly oriented cluster morphology with small aspect ratios (Fig. 20A and B). Meanwhile, A-Fe@CNF-3 exhibited fiber morphology (average fiber diameter was 238 nm) with a multinanorod twist structure, which comprised abundant winding nanorods with an average diameter of 47 nm (Fig. 20C and D). The formation of this multilevel structure could be attributed to the difference in the shrinkage rate between polybenzoxazine and PAN during the carbonization process [74]. To further study the multinanorod twist structure, the A-Fe@CNF-3 was broken into dispersed nanorods via high-speed stirring and characterized using TEM. As can be seen from Fig. 20E, the individual nanorod was comprised of porous graphitic carbon and embedded Fe_3O_4 nanocrystals with a grain size ranging from 5 to 20 nm. Careful examination of the corresponding HRTEM image (Fig. 20F) indicates the well-resolved lattice fringes with an interplane distance of 2.55 Å derived from the (311) plane of Fe_3O_4.

Here quantitative PSD analysis was achieved by employing the nonlocal density functional theory (NLDFT) method. The representative NLDFT PSD curves over the range of 2–25 nm revealed a typically polydisperse porous structure and a primary PSD in the range of 2–8 nm. Two well-developed peaks centered at 3.26 and 5.09 nm were observed in Fe@CNF samples. After activation, a new PSD peak centered at 2.46 nm arose, and the differential pore volumes of the relevant PSD peaks increased greatly, giving an indication of the significant enhancement of the mesoporous structure.

The detailed porous structure analysis showed that the specific surface area and the total pore volume of A-Fe@CNF increased greatly as compared to those of non-activated Fe@CNF samples. Another interesting result was

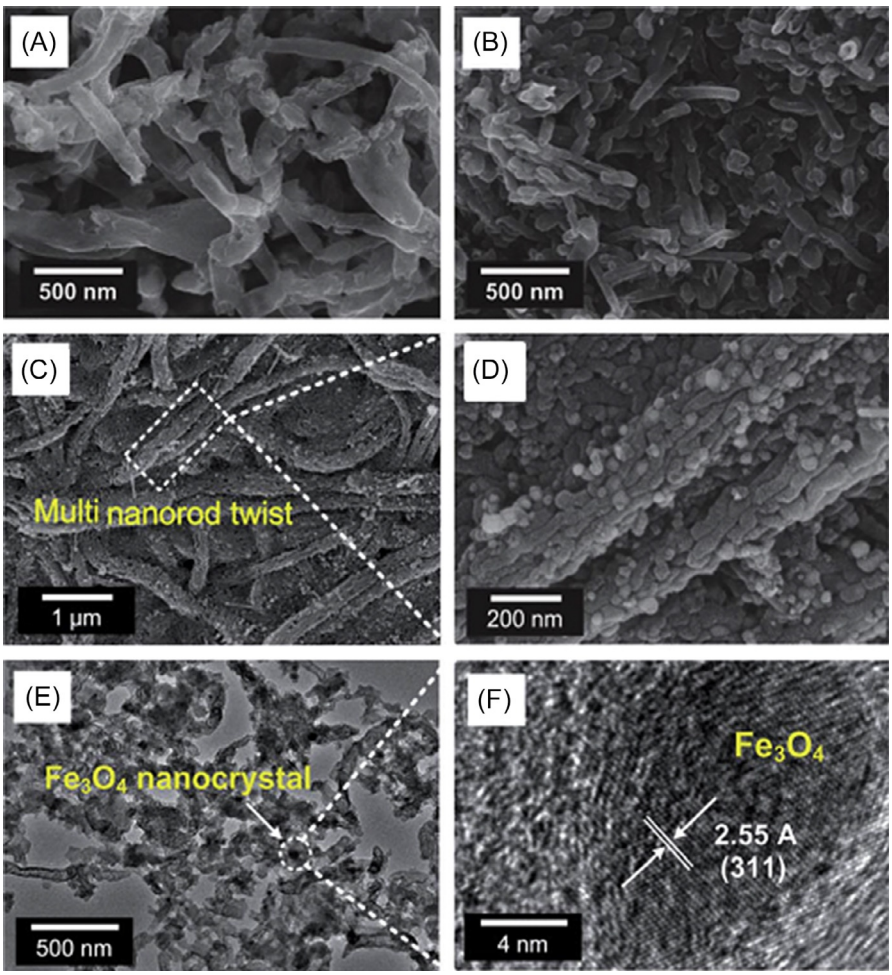

FIG. 20 FE-SEM images of (A) A-Fe@CNF-1 and (B) A-Fe@CNF-2. (C) Low and (D) high magnification FE-SEM images of A-Fe@CNF-3 showing the multinanorod twist structure. (E) TEM image of A-Fe@CNF-3. (F) HRTEM image showing Fe_3O_4 nanocrystals in (311) orientation embedded in carbon (A-Fe@CNF-3) [73].

that the mesopore volume fractions of all samples were higher than 75%, which confirmed the prevalence of mesopores in the nanofibers. Furthermore, it is worthwhile to point out that, by combination of precursor design and activation process, a series of Fe_3O_4@CNFs with tunable hierarchical porous structures, including the surface area, pore volume, and micro/mesopore ratio, were obtained, in which the A-Fe@CNF-3 possessed a remarkably high surface area of 1623 $m^2\ g^{-1}$ and a pore volume of 1.635 $cm^3\ g^{-1}$, which was higher than that of conventional PAN–based CNFs.

The adsorption performance of A-Fe@CNF-3 was tested with MB and RhB dye pollutants as well. The A-Fe@CNF-3 exhibited an excellent adsorption ability in the removal of MB and RhB dyes. The adsorption capacities of MB and RhB were 94% and 75% for 6 min, and could achieve complete adsorption of MB and RhB in 9 and 20 min, respectively. In addition, the relevant recycling results indicated that the adsorption capacities of MB and RhB were 91% and 83% after approximately eight cycles, respectively, revealing good recycling abilities for both dyes.

5 MCPBz NANOFIBERS

5.1 Main-Chain Nanofibers Obtained Without Blending With Other Polymeric Matrices

Ertas and Uyar reported the first study to produce bead-free and uniform polybenzoxazine nanofibers from MCPBz without using carrier polymeric matrices [75]. Initially, two different types of MCPBz (poly(BA-dh)$_{main}$ and poly(BA-dd)$_{main}$) were synthesized by using two types of difunctional amine (1,6-diaminohexane and 1,12-diaminododecane), BA, and paraformaldehyde as starting materials through a Mannich reaction. Then highly concentrated homogeneous solutions of the two MCPBzs in chloroform/*N*,*N*-dimethylformamide (DMF) (4:1, v/v) solvent system were prepared by varying the concentrations of poly(BA-dh)$_{main}$ (30–45%, w/v) and poly(BA-dd)$_{main}$ (15–20%, w/v). At low concentrated solutions, beaded ultrafine fibers were obtained. As the polymer concentration increased, the number of beads decreased dramatically and elongated beaded nanofibers were produced. When the polymer concentration reached critical value, transformation from beaded nanofibers to bead-free nanofibers was achieved, and the bead-free uniform nanofibers were obtained when poly(BA-dh)$_{main}$ and poly(BA-dd)$_{main}$ were electrospun and nanofibrous mats of these were at a solution concentration of 40% and 18% (w/v), respectively (Figs. 21 and 22). Poly(BA-dh)$_{main}$ and poly(BA-dd)$_{main}$ nanofibrous mats (poly(BA-dh)$_{main}$-FbM and poly(BA-dd)$_{main}$-FbM) were obtained as free-standing material, yet poly(BA-dd)$_{main}$-FbM was more flexible than and poly(BA-dh)$_{main}$-FbM, which possibly resulted from the longer diamine chain length and higher molecular weight of poly(BA-dd)$_{main}$ resin (Fig. 23A and B). The average fiber diameter and its distribution were calculated from scanning electron microscopy (SEM) images, and corresponding values were 745 ± 140 nm (between 400 and 1100 nm) and 805 ± 220 nm (between 400 and 1500 nm) for poly(BA-dh)$_{main}$-FbM and poly(BA-dd)$_{main}$-FbM, respectively (Figs. 21 and 22). Furthermore, curing studies on these nanofibrous mats give us a good starting point for cross-linking of MCPBz nanofibers. Although the fibrous structure could not be preserved during the thermal curing of poly(BA-dh)$_{main}$-FbM and poly(BA-dd)$_{main}$-FbM because of the low melting point of these MCPBz (Fig. 24), flexible and free-standing cross-linked films were obtained (Fig. 23C and D).

5.2 Cross-Linked, MCPBz Nanofibers by Photo and Thermal Curing

Ertas and Uyar first obtained cross-linked polybenzoxazine–based nanofibers from linear aliphatic diamine–based MCPBz by a two-step curing process: photo and thermal [76]. In their previous study, poly(BA-dh)$_{main}$ and poly(BA-dd)$_{main}$ nanofibers could not preserve the fibrous morphology during the thermal curing and melted at even very low temperatures (75–100°C). In order to enhance the thermal stability of nanofibers, the molecular structure of the poly(BA-dh)$_{main}$ and poly(BA-dd)$_{main}$ were slightly changed by tailoring the properties of the MCPBz to enable them to be photo curable. For this purpose, 4,4-dihydroxybenzophenone, which is a well-known photoinitiator used as difunctional phenolic derivative instead of BA and the other precursors, 1,6-diaminohexane, 1,12-diaminododecane and paraformaldehyde were used same as previous study. As a result, two novel MCPBzs, namely poly(DBP-dh)$_{main}$ and poly(DBP-dd)$_{main}$, were obtained from 6-C and 12-C aliphatic diamine, respectively (Fig. 25A). Their molecular weights were measured by GPC as ~10,000 and ~15,000 g mol^{-1}, respectively, which is expected since these MCPBz resins possess different chain lengths. The molecular structures of the poly(DBP-dh)$_{main}$ and poly(DBP-dd)$_{main}$ resins were confirmed by ^{1}H NMR. FTIR, and UV-Vis spectroscopies suggested that the synthesis of the desired MCPBz molecules were achieved.

Then homogenous solutions of poly(DBP-dh)$_{main}$ and poly(DBP-dd)$_{main}$ were prepared in a chloroform/DMF solvent mixture for the production of nanofibers by electrospinning (Fig. 25B). Solution concentrations varied between 25–35% (w/v) for poly(DBP-dh)$_{main}$ and 15–25% (w/v) for poly(DBP-dd)$_{main}$ in order to determine the optimum concentration. In the electrospinning process, polymeric systems exhibited typical behavior by transforming from beaded nanofibers to bead-free fibers when the concentration and/or

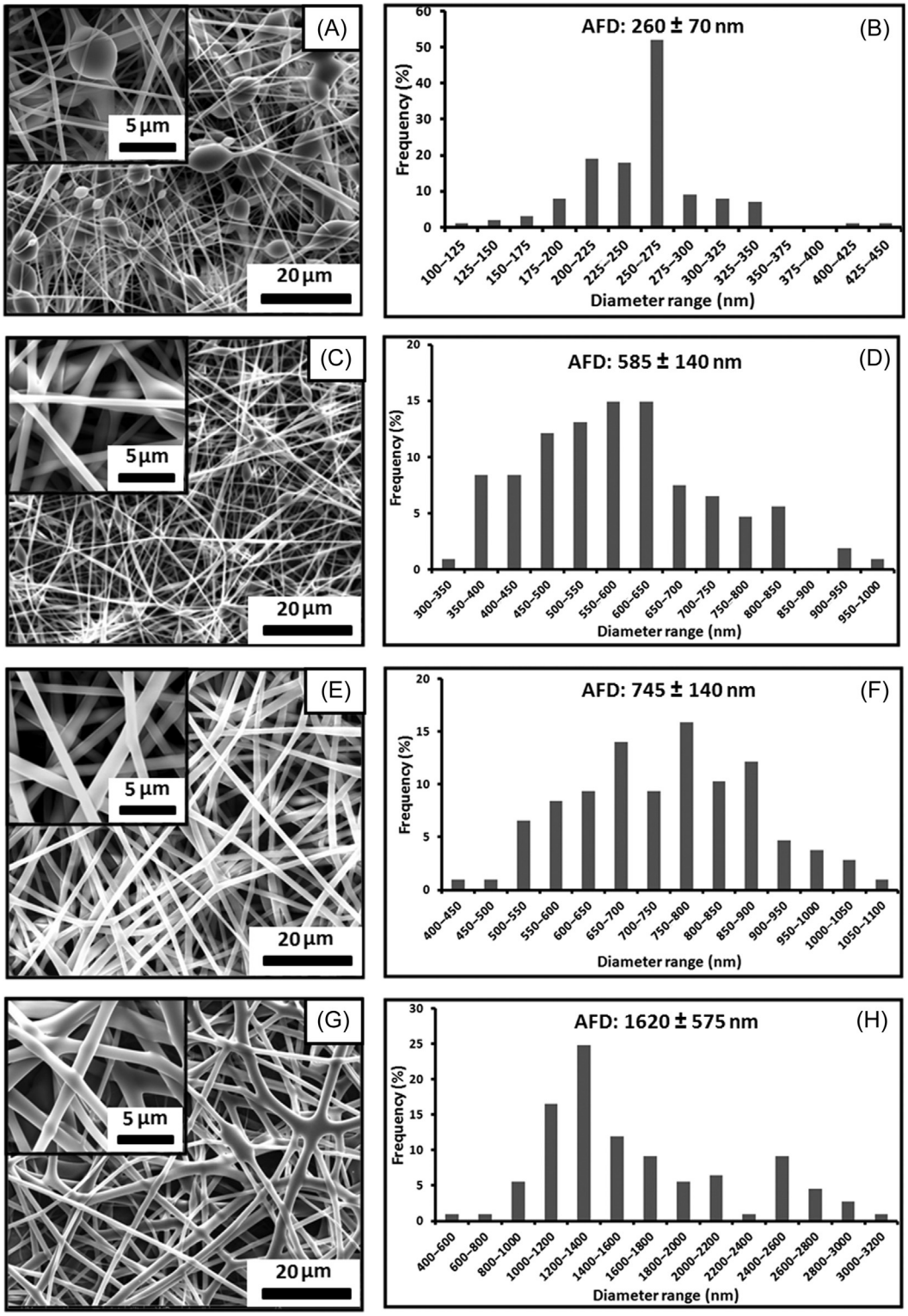

FIG. 21 Representative SEM images and corresponding fiber diameter distributions with average fiber diameter (AFD) of the electrospun nanofibers obtained from solutions of poly(BA-dh)$_{main}$ (A, B) 30%, (C, D) 35%, (E, F) 40%, and (G, H) 45%. Inset shows magnified view of a typical region [75].

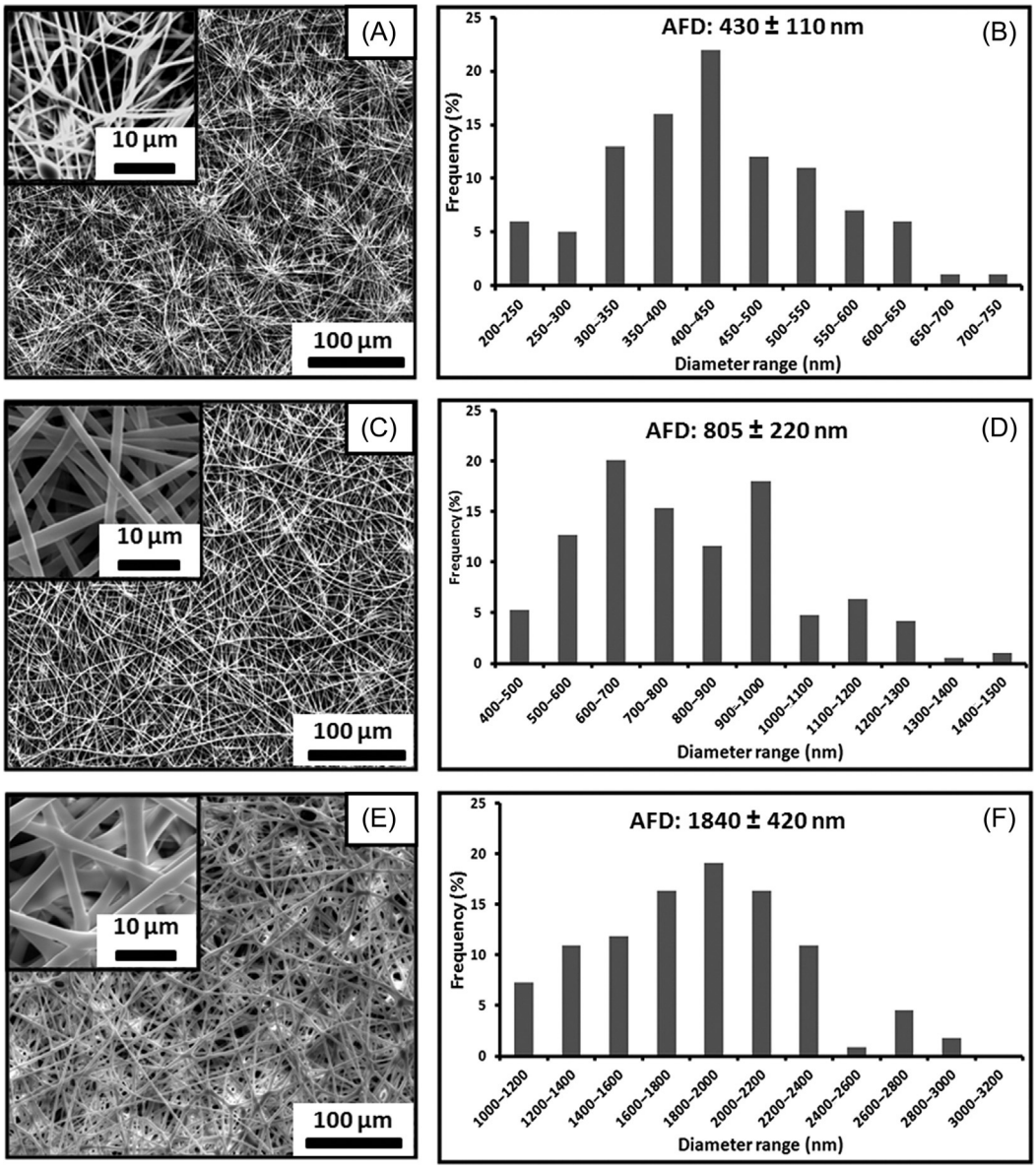

FIG. 22 Representative SEM images and corresponding fiber diameter distributions of the electrospun nanofibers obtained from solutions of poly(BA-dd)$_{main}$ (A, B) 15%, (C, D) 18%, and (E, F) 20%. Inset depicts magnified view of a typical region [75].

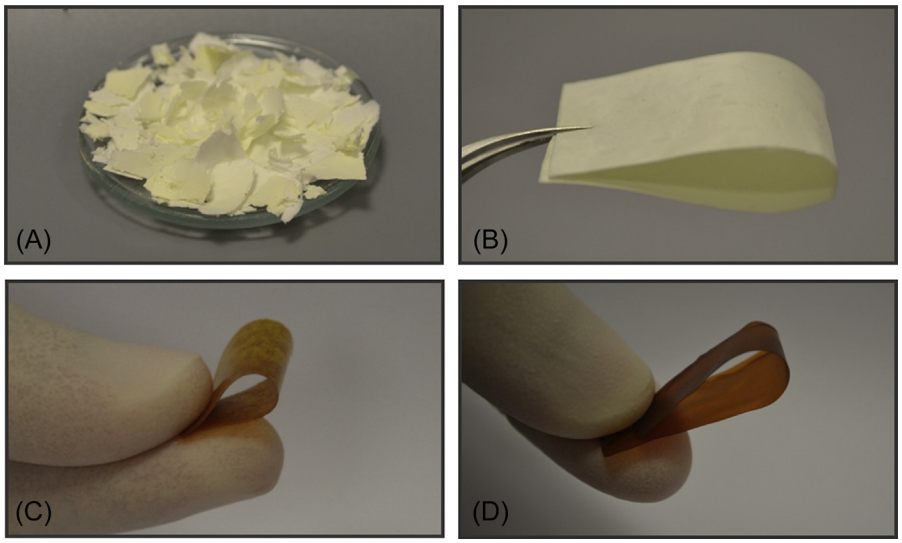

FIG. 23 Photographs of the (A) poly(BA-dh)$_{main}$-FbM, (B) poly(BA-dd)$_{main}$-FbM and after curing, (C) poly(BA-dh)$^{x}_{main}$, and (D) poly(BA-dd)$^{x}_{main}$ films step by step at 75°C, 1 h; 90°C, 1 h; 120°C, 1 h; 150°C, 1 h; 180°C, 1 h; and 220°C, 1 h [75].

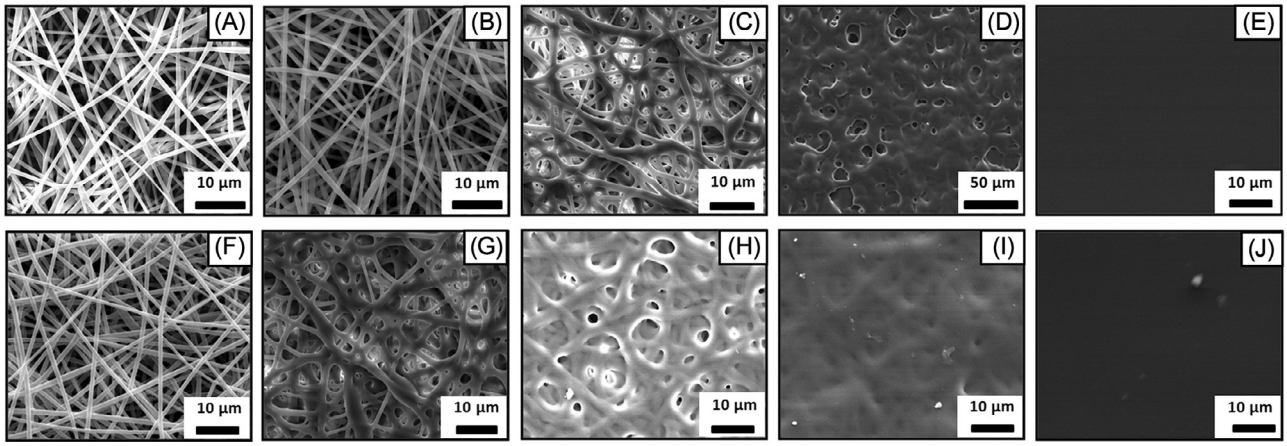

FIG. 24 Representative SEM images of the electrospun nanofibers before and after thermal treatment: (A) 40% poly(BA-dh)$_{main}$; (B) 75°C, 1 h; (C) 90°C, 1 h; (D) 100°C; 1 h; (E) 120°C, 1 h; (F) 18% poly(BA-dd)$_{main}$; (G) 50°C, 1 h; (H) 60°C,1 h; (I) 75°C, 1 h; and (J) 120°C, 1 h [75].

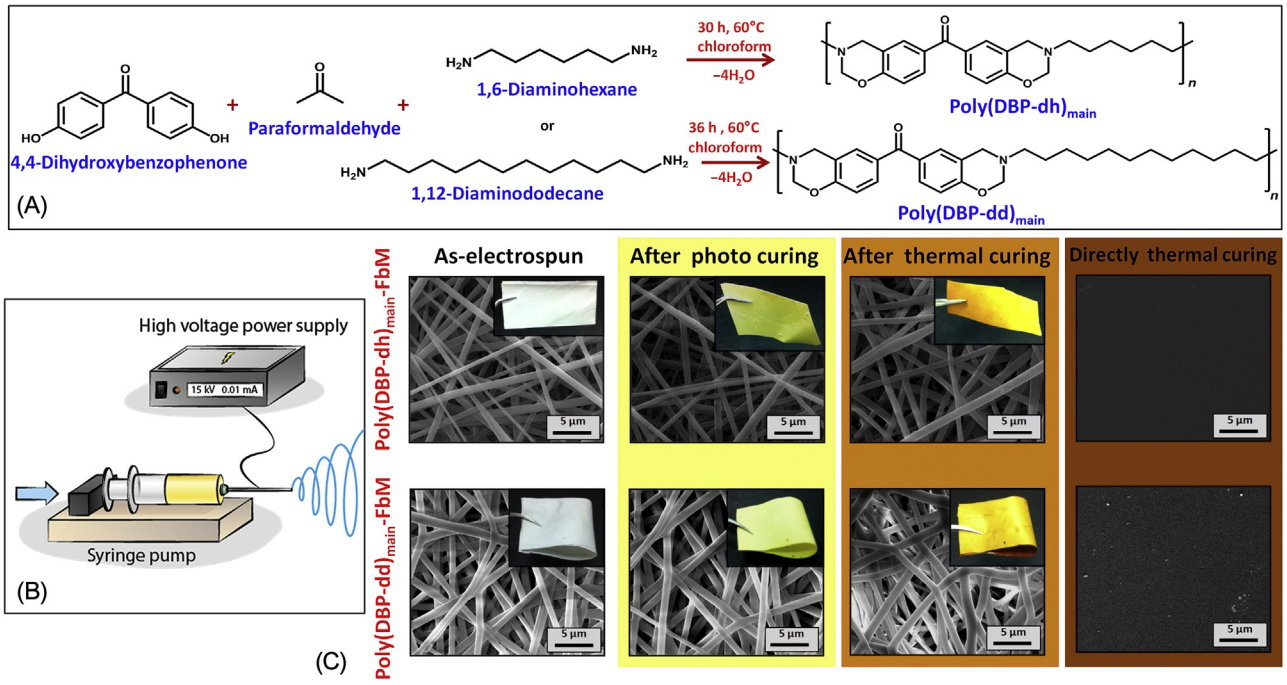

FIG. 25 (A) Synthesis mechanisms of the poly(DBP-dh)$_{main}$ and poly(DBP-dd)$_{main}$ resins; (B) schematic view of the electrospinning setup; and (C) SEM images of poly(DBP-dh)$_{main}$-FbM and poly(DBP-dd)$_{main}$-FbM before and after curing. Inset depicts photographs of the nanofibrous mat for corresponding SEM image [76].

viscosity of the polymer solution was optimized. Naturally, the aliphatic diamine chain length and accordingly the molecular weight of the MCPBz resins affected the electrospinning ability. Because poly(DBP-dd)$_{main}$ resin has a higher molecular weight and a longer aliphatic chain, presumably more chain entanglement and overlapping occurred in the polymer solution, thus resulting in the formation of bead-free and uniform nanofibers at a lower solution concentration (25%, w/v), compared to the poly(DBP-dh)$_{main}$ (35%, w/v). Both nanofibrous mats were obtained as free-standing material, yet poly(DBP-dd)$_{main}$-FbM was more flexible than the poly(DBP-dh)$_{main}$-FbM, most likely because of the different chain length of these two MCPBzs.

Curing experiments of poly(DBP-dh)$_{main}$-FbM and poly(DBP-dd)$_{main}$-FbM were performed in a two-step process in order to obtain cross-linked MCPBz nanofibers without deteriorating the fiber morphology. First, photo curing was carried out by irradiating nanofibrous mats with UV-light for 1 h to achieve preliminary cross-linking. DSC experiments were conducted to measure the thermal transition

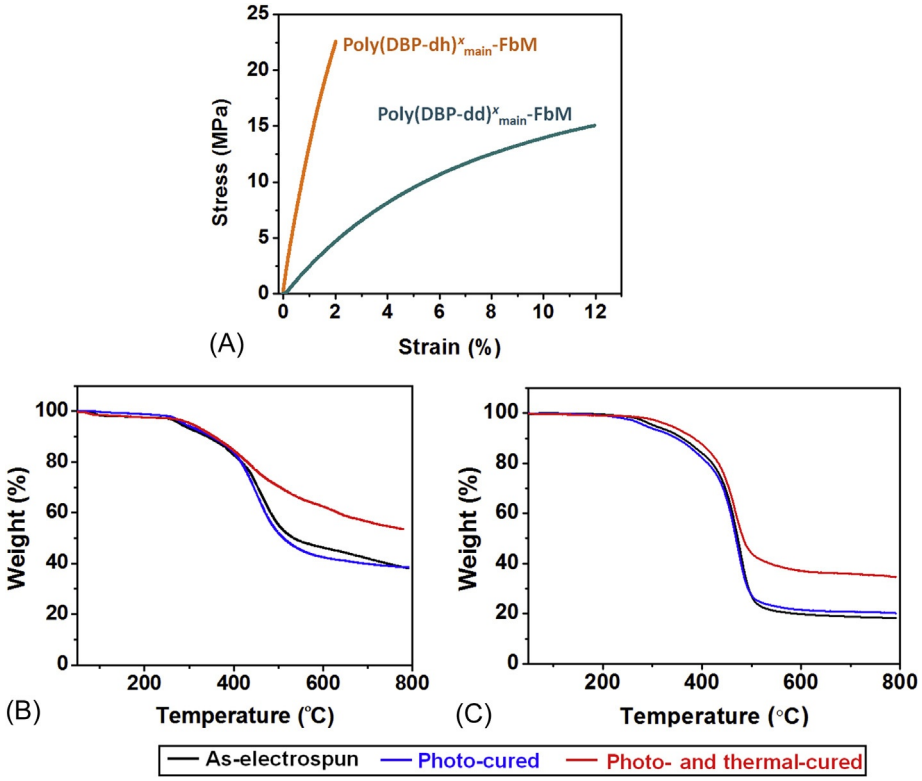

FIG. 26 (A) DMA curves of poly(DBP-dh)$^{x}_{main}$-FbM and poly(DBP-dd)$^{x}_{main}$-FbM, TGA thermograms of (B) poly(DBP-dh)$_{main}$-FbM and (C) poly(DBP-dd)$_{main}$-FbM before and after curing [76].

temperatures of the samples before and after curing. Interestingly, the melting transition peak of both as-electrospun MCPBz nanofibers disappeared after the photo curing, indicating the enhancement of the thermal stability of nanofibers. Second, thermal curing was performed by keeping the photo-cured samples at different temperatures (150°C, 175°C, 200°C, and 225°C) for 1 h in a standard oven to provide ring-opening and cross-linking of the oxazine molecule in the main-chain; consequently, cross-linked poly(DBP-dh)$^{x}_{main}$ and poly(DBP-dd)$^{x}_{main}$ nanofibrous mats were fabricated. In addition, as-electrospun MCPBz nanofibers were directly thermal-cured without the photo curing step as a control experiment. SEM images showed that, although directly thermal-cured MCPBz nanofibers lost their fibrous structure even during the first step (150°C) of the thermal curing, photo-cured nanofibers perfectly preserved the fiber morphology throughout the thermal curing process, confirming the accomplishment of cross-linking without deteriorating the fiber morphology in only two steps (Fig. 25C). Moreover, molecular structural changes occurring during the two-step curing process were investigated by FTIR spectroscopy, and characteristic absorption peaks of the benzoxazine ring disappeared with thermal curing, verifying the achievement of ring-opening and cross-linking.

Furthermore, mechanical properties of the poly(DBP-dh)$^{x}_{main}$-FbM and poly(DBP-dd)$^{x}_{main}$-FbM were investigated by dynamic mechanical analyzer (DMA). Stress-strain curves of both cross-linked MCPBz nanofibrous mats are shown in Fig. 26A. After two-step curing, poly(DBP-dh)$^{x}_{main}$-FbM and poly(DBP-dd)$^{x}_{main}$-FbM showed remarkably high Young's modulus (2070 ± 243 and 264 ± 59.66 MPa, respectively) and stress at yield (22.53 ± 2.04 and 15.29 ± 2.48 MPa, respectively) compared to the directly thermal-cured MCPBz nanofibrous mats reported in the literature [77]. Stress at yield and corresponding stiffness of the polymeric material depends on the chain length. Namely, as the flexible aliphatic chain length decreases, stiffness of the polymeric materials increases [39], thus poly(DBP-dh)$^{x}_{main}$-FbM showed notably higher Young's modulus and stress at yield than the poly(DBP-dd)$^{x}_{main}$-FbM. On the other hand, poly(DBP-dd)$^{x}_{main}$-FbM showed significantly higher strain at break (12.04 ± 0.09) compared to the poly(DBP-dh)$^{x}_{main}$-FbM (1.83 ± 0.15) because of the longer aliphatic diamine; as the aliphatic chain length increases, strain at break increases as well, and these results are consistent with the reported data [13].

In addition, thermal properties of poly(DBP-dh)$^{x}_{main}$-FbM and poly(DBP-dd)$^{x}_{main}$-FbM were examined by thermogravimetric analyzer (TGA). Td temperatures of the as-electrospun MCPBz nanofibrous mat shifted to higher temperatures, and the char yields of these materials

significantly increased after two-step curing (Fig. 26B and C). Corresponding values of Td onset, Td maximum, and char yield for the poly(DBP-dh)$^{x}_{main}$-FbM and poly(DBP-dd)$^{x}_{main}$-FbM were measured as 250°C, 458°C, 53.1%, and 270°C, 476°C, 35.1%, respectively, which are quite satisfying results for such materials.

Moreover, the thermal stability of poly(DBP-dh)$^{x}_{main}$-FbM and poly(DBP-dd)$^{x}_{main}$-FbM were tested in a temperature range between 250°C and 400°C in which higher than the curing temperature and lower than the decomposition temperature. Interestingly, poly(DBP-dh)$^{x}_{main}$-FbM and poly(DBP-dd)$^{x}_{main}$-FbM absolutely keep the same fiber morphology even after thermal treatment at 400°C (Fig. 27). Also, solubility and stability experiments were performed in good solvents (chloroform, DMF, 1,4-dioxane,*N*,*N*-dimethylacrylamide (DMAc), and tetrahydrofuran (THF)) and highly concentrated, (5 M) strong acid (HCl, HNO_3, H_2SO_4) solutions. SEM images of poly(DBP-dh)$^{x}_{main}$-FbM and poly(DBP-dd)$^{x}_{main}$-FbM, after immersion overnight in mentioned solvents and strong acids, demonstrated that these nanofibers preserved their fibrous structure and mechanical integrity perfectly after two-step curing (Figs. 28 and 29). In conclusion, here highly cross-linked thermoset nanofibrous polybenzoxazine–based materials with quite good mechanical and thermal properties were produced by two-step curing. Also, these materials are highly stable in organic solvents and harsh acidic conditions. All these outstanding properties of the poly(DBP-dh)$^{x}_{main}$-FbM and poly(DBP-dd)$^{x}_{main}$-FbM may be quite useful for the certain applications requiring high temperatures and harsh acidic conditions or organic solvents.

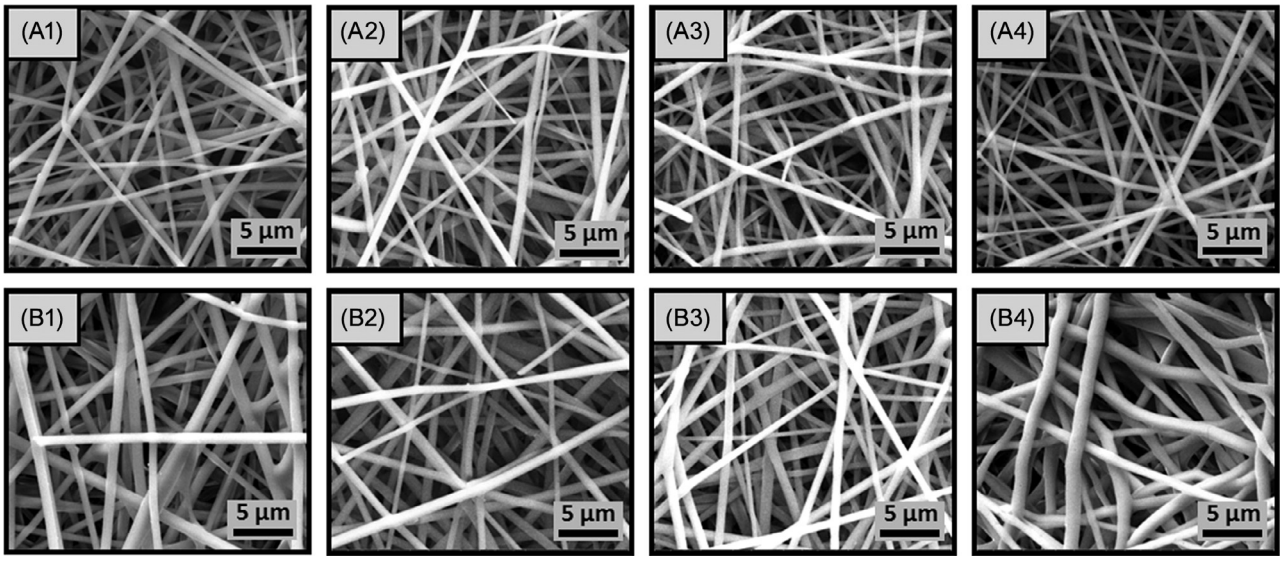

FIG. 27 SEM images of (A) poly(DBP-dh)$^{x}_{main}$-FbM and (B) poly(DBP-dd)$^{x}_{main}$-FbM after treating different temperatures in high temperature tube furnace at open air: (1) 250°C (1 h); (2) 300°C (0.5 h); (3) 350°C (0.5 h); and (4) 400°C (0.5 h) [76].

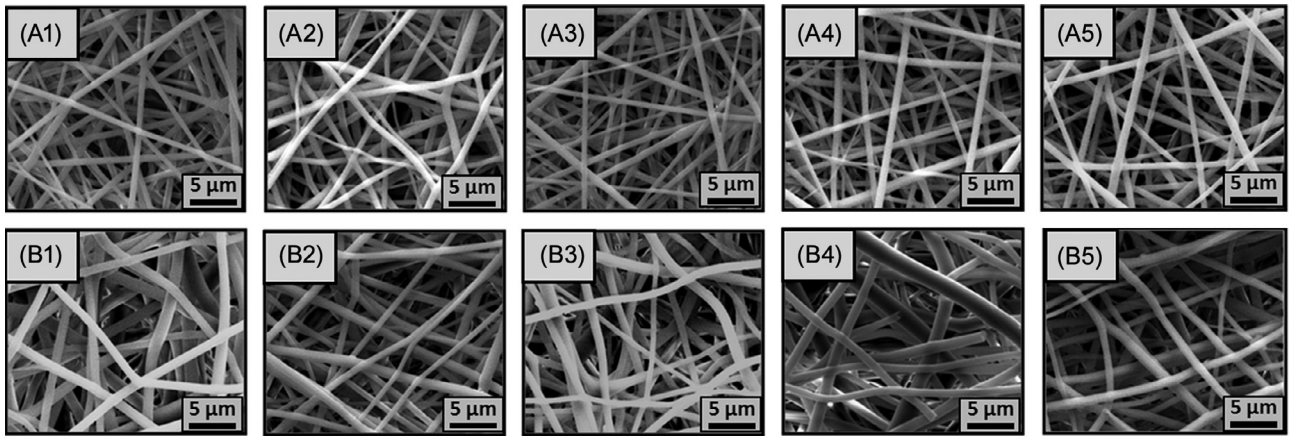

FIG. 28 SEM images of (A) poly(DBP-dh)$^{x}_{main}$-FbM and (B) poly(DBP-dd)$^{x}_{main}$-FbM after immersing 24 h in (1) chloroform; (2) DMF; (3) 1,4-dioxane; (4) DMAc; and (5)THF [76].

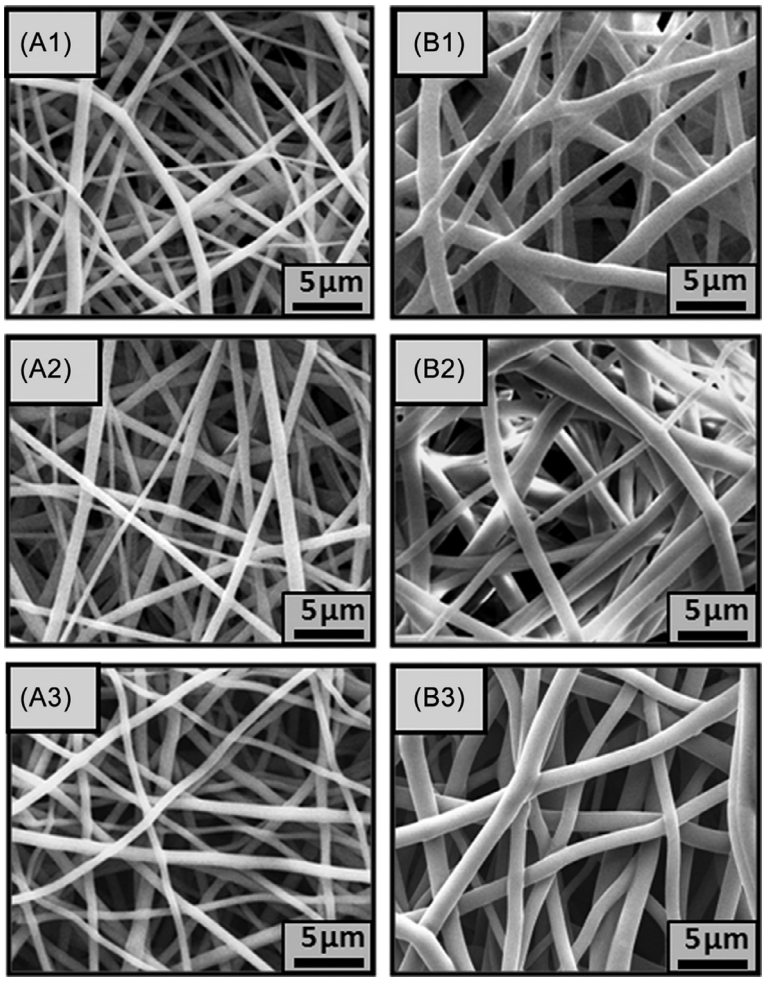

FIG. 29 SEM images of (A) poly(DBP-dh)$^{x}_{main}$-FbM and (B) poly(DBP-dd)$^{x}_{main}$-FbM after immersing 24 h in 5 M (1) HCl, (2) HNO_3, and (3) H_2SO_4 solutions [76].

5.3 Robust Blood-Inert and Shape-Reproducible Electrospun MCPBz Nanofibrous Mats

Recently, Li and coworkers produced cross-linked MCPBz nanofibers by thermal curing, and they demonstrated that these cross-linked nanofibers are robustly blood-inert and shape-reproducible [77]. Blood-inertness is known as the resistance of the surfaces to the adsorption of plasma proteins and the adhesion of the blood cells, which is a quite desirable and very important characteristic while developing blood-contacting materials such as blood collection devices, antithrombogenic implants, hemodialysis membranes, drug-delivery carriers, and diagnostic biosensors [78,79]. Inherent surface contact stimulates the thrombotic reaction, which is strongly affected by the interactions of clotting factors, plasma proteins, and platelets on blood-contacting materials [80]. Nonspecific adsorption of proteins and clotting enzymes at the blood-material interface is understood as being the first interaction event to stimulate a fullscale platelet adhesion, and activation causes thrombosis and embolism at the blood-material interface [81]. Therefore development of materials with protein-resistant surfaces to prevent blood clot formation is crucial and is widely studied in the literature. However, most of the methods require complicated processes such as chemical reactions, physical adsorption, and alteration of surface topography, which cause surfaces to have poor mechanical properties and less resistance to harsh environmental conditions. On the other hand, a recent study introduced a new approach by combining the electrospinning and in situ polymerization/cross-linking of MCPBz for the fabrication of blood-inert materials without further surface modification. Initially, MCPBz resin poly(BA-dpe)$_{main}$ was synthesized by using 4,4′-diaminophenylether, BA, and formaldehyde as raw materials. During the electrospinning, the concentration of the feeding poly(BA-dpe)$_{main}$ solution was optimized to be 28 wt% in a mixed solvent system of THF and DMSO (v/v = 3/1), and bead-free nanofibers were produced with an average fiber diameter of about 1.9 µm. The obtained

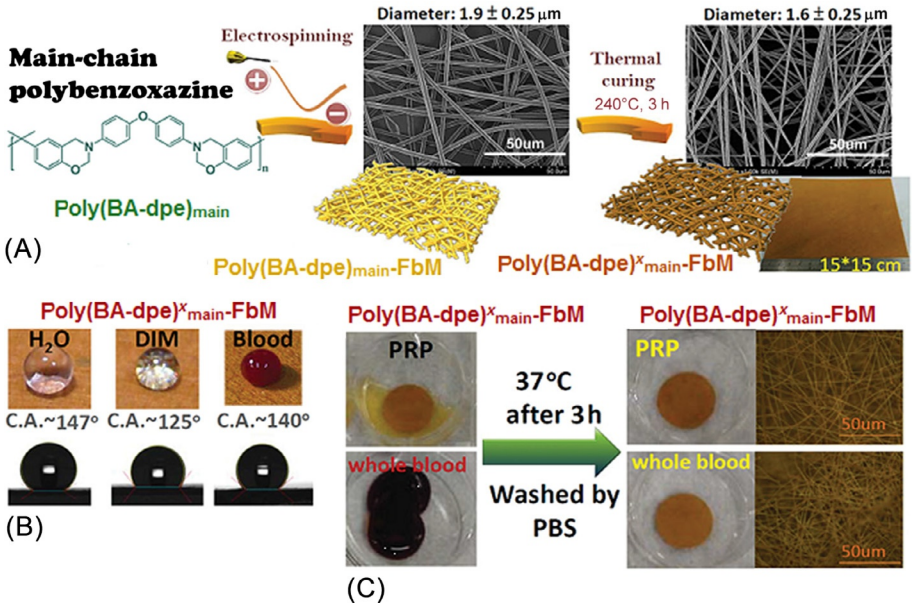

FIG. 30 (A) Preparation of blood-inert material with an electrospinning process using a main-chain polybenzoxazine as raw material. The electrospun poly(BA-dpe)$_{main}$-FbM can be thermally cured without altering its morphology; (B) the contact angles of poly(BA-dpe)$^{x}_{main}$-FbM measured with water, DIM, and whole human blood (WHB) were 147, 125, and 140 degrees, respectively; and (C) poly(BA-dpe)$^{x}_{main}$-FbM shows high blood inertness because no blood cell attachment was observed on the sample in contact with platelet–rich plasma (PRP) and WHB by fluorescence microscopy [77].

poly(BA-dpe)$_{main}$ nanofibrous mats were thermally cured at 200°C for 1 h and 240°C for 3 h, and cross-linked poly(BA-dpe)$_{main}$ fibrous mats (poly(BA-dpe)$^{x}_{main}$-FbM) were produced with preserved fiber structures (Fig. 30A), because the melting point of poly(BA-dpe)$_{main}$ is higher than the curing temperature (240°C). Interestingly, poly(BA-dpe)$^{x}_{main}$-FbM exhibits some attractive properties without further surface modification and treatments. First, poly(BA-dpe)$^{x}_{main}$-FbM shows a WCA of about 147 degrees and a diiodinemethane (DIM) contact angle of about 125 degrees (Fig. 30B), which shows a higher amphiphobic characteristic compared to the cross-linked polybenzoxazine film (WCA: 108 degrees and DIM: 51 degrees) owing to the low-surface energy of cross-linked polybenzoxazine and the surface roughness of the electrospun fiber structure. Also, the amphiphobic poly(BA-dpe)$^{x}_{main}$-FbM shows a contact angle of about 140 degrees for whole human blood (WHB). The blood-inert characteristics and blood cell attachment resistance of poly(BA-dpe)$^{x}_{main}$-FbM samples were tested by direct immersion in blood platelet–rich plasma and undiluted WHB for 3 h at 37°C, respectively. Then samples were washed with a phosphate-buffered saline solution. It was observed that poly(BA-dpe)$^{x}_{main}$-FbM showed complete resistance to platelet adhesion and that no blood cells were observed to attach on the surface of poly(BA-dpe)$^{x}_{main}$-FbM sample, illustrating the excellent blood-inertness with almost 100-percent resistance to blood cell attachment (Fig. 30C). Here the blood-inertness of poly(BA-dpe)$^{x}_{main}$-FbM can be attributed mainly to low-surface-free-energy and consequently to the hydrophobicity of this material.

The robustness of the surface characteristics of poly(BA-dpe)$^{x}_{main}$-FbM has been examined by mechanical testing, in various organic solvents (THF, EtOH, acetone, toluene, and *n*-hexane) and aqueous solutions with different pH values (Fig. 31). The WCA of poly(BA-dpe)$^{x}_{main}$-FbM was almost unchanged after the mechanical test, indicating that the surface characteristics of poly(BA-dpe)$^{x}_{main}$-FbM are mechanically resistant. Moreover, in organic solvents, poly(BA-dpe)$^{x}_{main}$-FbM samples were neither dissolved nor highly swollen in the solvents because of the highly cross-linked structure and did not show notable changes in the measured WCAs. This result demonstrates the high solvent resistance of poly(BA-dpe)$^{x}_{main}$-FbM, which is able to maintain its surface characteristics in contact with solvents. In addition, after immersing poly(BA-dpe)$^{x}_{main}$-FbM samples in the different pH media, they had almost the same WCA measurement, except for pH 1 and 13, presumably, harsh environmental conditions altered the chemical structures of the sample surface because of the protonation and deprotonation reactions of the hydroxyl and amine groups of the cross-linked PBz structure, respectively. Lastly, poly(BA-dpe)$^{x}_{main}$-FbM could maintain the surface characteristics up to 250°C, demonstrating the thermal stability of samples.

Poly(BA-dpe)$^{x}_{main}$-FbM possesses shape recovery ability, and reshaping the shaped poly(BA-dpe)$^{x}_{main}$-FbM sample to either another shape or to the original shape is possible under force (Fig. 32A). Poly(BA-dpe)$^{x}_{main}$-FbM shows a Young's modulus of 167 ± 48 MPa, a stress

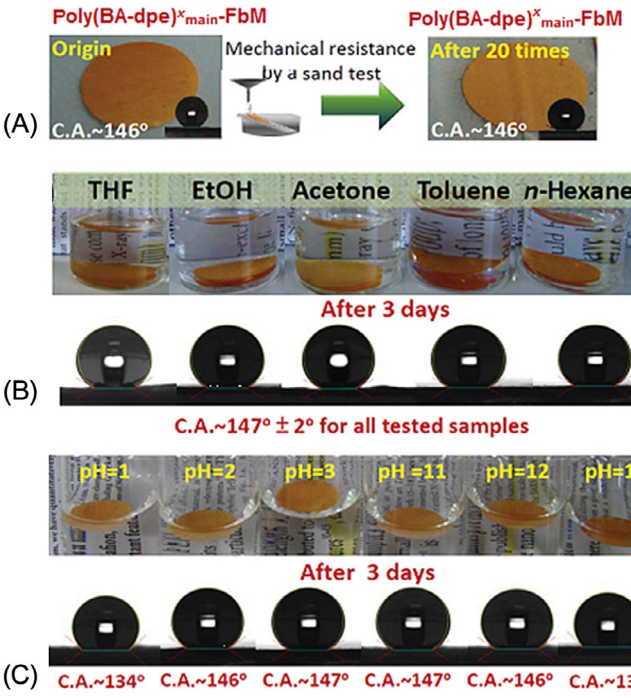

FIG. 31 Tests on the robustness of poly(BA-dpe)$^{x}_{main}$-FbM. (A) Mechanical resistance by a sand abrasion test 9 in which there were no changes of water WCA of poly(BA-dpe)$^{x}_{main}$-FbM after a 20-run test; (B) solvent-resistance test in which there were no changes of WCA of poly(BA-dpe)$^{x}_{main}$-FbM after being soaked in various solvents for 3 days; and (C) pH resistance test in which poly(BA-dpe)$^{x}_{main}$-FbM was stable after being soaked in pH 2–12 aqueous solutions. A slight decrease in WCA from 147 degrees to about 133 degrees was observed in the harsh pH 1 and 13 tests [77].

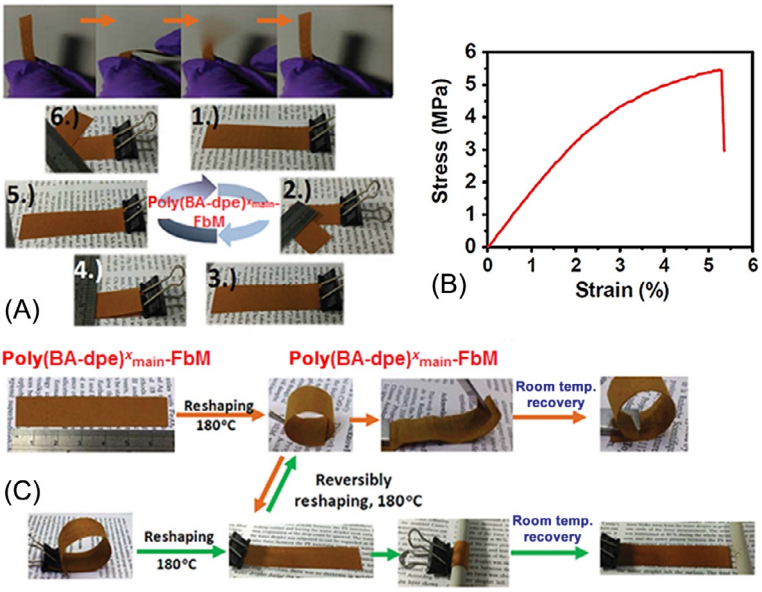

FIG. 32 (A) High mechanical strength flexibility of poly(BA-dpe)$^{x}_{main}$-FbM; (B) stress-strain curve recorded with poly(BA-dpe)$^{x}_{main}$-FbM; and (C) shape reformability and reproducibility of poly(BA-dpe)$^{x}_{main}$-FbM under a thermal treatment [77].

strength of 5.3 ± 0.1 MPa, and an elongation at break of 5.3 ± 0.2% (Fig. 32B). Reshaping the shaped poly(BA-dpe)$^{x}_{main}$-FbM sample to either another shape or the original shape is possible under force and heat. The poly(BA-dpe)$^{x}_{main}$-FbM sample in the new shape still exhibit flexibility and shape-recovery ability with forces at room temperature (Fig. 32C). However, the reshaped poly(BA-dpe)$^{x}_{main}$-FbM could not thermoresponsively recover the original shape because of the highly cross-linked structure and high T_g of poly(BA-dpe)$^{x}_{main}$-FbM.

6 SUMMARY

In this chapter, the recent progress in the preparation of polybenzoxazine–based nanofibrous mats has been reviewed. In situ polymerization of benzoxazine monomers allows both the surface modification of nanofibrous mat and the production of polybenzoxazine–based composite nanofibers. In addition, by taking advantage of the molecular design flexibility of polybenzoxazine, polybenzoxazine nanofibers have been obtained without blending with polymeric carrier

matrices. Because of the simplicity and versatility of the electrospinning, functional nanofibrous mats based on polybenzoxazine can be produced easily, and these materials have great potential in various applications.

ACKNOWLEDGMENTS

Dr. T. Uyar acknowledges The Turkish Academy of Sciences - Outstanding Young Scientists Award Program (TUBA-GEBIP) for partial funding. Y. Ertas acknowledges TUBITAK (2211-C) for the PhD student scholarship.

REFERENCES

[1] J. Sun, W. Wei, Y. Xu, J. Qu, X. Liu, T. Endo, A curing system of benzoxazine with amine: reactivity, reaction mechanism and material properties, RSC Adv. 5 (2015) 19048–19057.

[2] C. Li, Q. Ran, R. Zhu, Y. Gu, Study on thermal degradation mechanism of a cured aldehyde-functional benzoxazine, RSC Adv. 5 (2015) 22593–22600.

[3] P. Yang, Y. Gu, A novel benzimidazole moiety-containing benzoxazine: synthesis, polymerization, and thermal properties, J. Polym. Sci. A Polym. Chem. 50 (2012) 1261–1271.

[4] H. Zhang, W. Gu, R. Zhu, Q. Ran, Y. Gu, Study on the thermal degradation behavior of sulfone-containing polybenzoxazines via Py-GC-MS, Polym. Degrad. Stab. 111 (2015) 38–45.

[5] P. Yang, X. Wang, H. Fan, Y. Gu, Effect of hydrogen bonds on the modulus of bulk polybenzoxazines in the glassy state, Phys. Chem. Chem. Phys. 15 (2013) 15333–15338.

[6] W.-K. Kim, W.L. Mattice, Molecular modeling of a thin film of polybenzoxazine, Langmuir 14 (1998) 6588–6593.

[7] T. Feng, J. Wang, H. Wang, N. Ramdani, L. Zu, W. Liu, X. Xu, Copolymerization of fluorene-based main-chain benzoxazine and their high performance thermosets, Polym. Adv. Technol. 26 (2015) 581–588.

[8] C.H. Lin, Y.S. Shih, M.W. Wang, C.Y. Tseng, T.Y. Juang, C.F. Wang, Emission and surface properties of main-chain type polybenzoxazine with pyridinyl moieties, RSC Adv. 4 (2014) 8692–8698.

[9] B. Kiskan, Y. Yagci, Self-healing of poly (propylene oxide)-polybenzoxazine thermosets by photoinduced coumarine dimerization, J. Polym. Sci. A Polym. Chem. 52 (2014) 2911–2918.

[10] J. Shi, X. Zheng, L. Xie, F. Cao, Y. Wu, W. Liu, Film-forming characteristics and thermal stability of low viscosity benzoxazines derived from melamine, Eur. Polym. J. 49 (2013) 4054–4061.

[11] J. Liu, X. Lu, Z. Xin, C. Zhou, Synthesis and surface properties of low surface free energy silane-functional polybenzoxazine films, Langmuir 29 (2012) 411–416.

[12] K. Zhang, Q. Zhuang, Y. Zhou, X. Liu, G. Yang, Z. Han, Preparation and properties of novel low dielectric constant benzoxazole-based polybenzoxazine, J. Polym. Sci. A Polym. Chem. 50 (2012) 5115–5123.

[13] A.D. Baranek, L.L. Kendrick, J. Narayanan, G.E. Tyson, S. Wand, D.L. Patton, Flexible aliphatic-bridged bisphenol-based polybenzoxazines, Polym. Chem. 3 (2012) 2892–2900.

[14] C.H. Lin, S.L. Chang, T.Y. Shen, Y.S. Shih, H.T. Lin, C.F. Wang, Flexible polybenzoxazine thermosets with high glass transition temperatures and low surface free energies, Polym. Chem. 3 (2012) 935–945.

[15] L. Qu, Z. Xin, Preparation and surface properties of novel low surface free energy fluorinated silane-functional polybenzoxazine films, Langmuir 27 (2011) 8365–8370.

[16] A. Tuzun, B. Kiskan, N. Alemdar, A.T. Erciyes, Y. Yagci, Benzoxazine containing polyester thermosets with improved adhesion and flexibility, J. Polym. Sci. A Polym. Chem. 48 (2010) 4279–4284.

[17] M. Nakamura, H. Ishida, Synthesis and properties of new cross-linkable telechelics with benzoxazine moiety at the chain end, Polymer 50 (2009) 2688–2695.

[18] B. Kiskan, Y. Yagci, H. Ishida, Synthesis, characterization, and properties of new thermally curable polyetheresters containing benzoxazine moieties in the main chain, J. Polym. Sci. A Polym. Chem. 46 (2008) 414–420.

[19] T. Takeichi, T. Kano, T. Agag, Synthesis and thermal cure of high molecular weight polybenzoxazine precursors and the properties of the thermosets, Polymer 46 (2005) 12172–12180.

[20] P. Lorjai, S. Wongkasemjit, T. Chaisuwan, A.M. Jamieson, Significant enhancement of thermal stability in the non-oxidative thermal degradation of bisphenol-A/aniline based polybenzoxazine aerogel, Polym. Degrad. Stab. 96 (2011) 708–718.

[21] S. Mahadik-Khanolkar, S. Donthula, A. Bang, C. Wisner, C. Sotiriou-Leventis, N. Leventis, Polybenzoxazine aerogels. 2. Interpenetrating networks with iron oxide and the carbothermal synthesis of highly porous monolithic pure iron (0) aerogels as energetic materials, Chem. Mater. 26 (2014) 1318–1331.

[22] D.A. Rubenstein, H. Lu, S.S. Mahadik, N. Leventis, W. Yin, Characterization of the physical properties and biocompatibility of polybenzoxazine-based aerogels for use as a novel hard-tissue scaffold, J. Biomater. Sci. Polym. Ed. 23 (2012) 1171–1184.

[23] T. Chaisuwan, T. Komalwanich, S. Luangsukrerk, S. Wongkasemjit, Removal of heavy metals from model wastewater by using polybenzoxazine aerogel, Desalination 256 (2010) 108–114.

[24] P. Katanyoota, T. Chaisuwan, A. Wongchaisuwat, S. Wongkasemjit, Novel polybenzoxazine-based carbon aerogel electrode for supercapacitors, Mater. Sci. Eng. B 167 (2010) 36–42.

[25] P. Lorjai, T. Chaisuwan, S. Wongkasemjit, Porous structure of polybenzoxazine-based organic aerogel prepared by sol-gel process and their carbon aerogels, J. Sol-Gel Sci. Technol. 52 (2009) 56–64.

[26] O.S. Taskin, B. Kiskan, A. Aksu, N. Balkis, J. Weber, Y. Yagci, Polybenzoxazine: a powerful tool for removal of mercury salts from water, Chem. Eur. J. 20 (2014) 10953–10958.

[27] K. Pakkethati, N. Tungsattabutrat, T. Chaisuwan, S. Wongkasemjit, High performance of polybenzoxazine membranes for ethanol-water separation via pervaporation technique, Mater. Res. Innov. 16 (2012) 243–248.

[28] Y. Shang, Y. Si, A. Raza, L. Yang, X. Mao, B. Ding, J. Yu, An *in situ* polymerization approach for the synthesis of superhydrophobic and superoleophilic nanofibrous membranes for oil-water separation, Nanoscale 4 (2012) 7847–7854.

[29] X. Tang, Y. Si, J. Ge, B. Ding, L. Liu, G. Zheng, W. Luo, J. Yu, *In situ* polymerized superhydrophobic and superoleophilic nanofibrous membranes for gravity driven oil-water separation, Nanoscale 5 (2013) 11657–11664.

[30] L. Yang, A. Raza, Y. Si, X. Mao, Y. Shang, B. Ding, J. Yu, S.S. Al-Deyab, Synthesis of superhydrophobic silica nanofibrous membranes with robust thermal stability and flexibility via *in situ* polymerization, Nanoscale 4 (2012) 6581–6587.

[31] V.A. Ganesh, H.K. Raut, A.S. Nair, S. Ramakrishna, A review on self-cleaning coatings, J. Mater. Chem. 21 (2011) 16304–16322.

[32] J. Lin, Y. Cai, X. Wang, B. Ding, J. Yu, M. Wang, Fabrication of biomimetic superhydrophobic surfaces inspired by lotus leaf and silver ragwort leaf, Nanoscale 3 (2011) 1258–1262.
[33] X. Liu, Y. Liang, F. Zhou, W. Liu, Extreme wettability and tunable adhesion: biomimicking beyond nature? Soft Matter 8 (2012) 2070–2086.
[34] X. Wang, B. Ding, J. Yu, M. Wang, Engineering biomimetic superhydrophobic surfaces of electrospun nanomaterials, Nanotoday 6 (2011) 510–530.
[35] K.F.S. Ramakrishna, W. Teo, T. Lim, Z. Ma, An Introduction to Electrospinning and Nanofibers, World Scientific Publishing Company, Singapore, 2005.
[36] J.H. Wendorff, S. Agarwal, A. Greiner, Electrospinning: Materials, Processing, and Applications, Wiley-VCH, Germany, 2012.
[37] A. Greiner, J.H. Wendorff, Electrospinning: a fascinating method for the preparation of ultrathin fibres, Angew. Chem. Int. Ed. 46 (2007) 5670–5703.
[38] J.P.F. Lagerwall, J.T. McCann, E. Formo, G. Scalia, Y.N. Xia, Coaxial electrospinning of microfibres with liquid crystal in the core, Chem. Commun. (2008) 5420–5422.
[39] S. Agarwal, J.H. Wendorff, A. Greiner, Chemistry on electrospun polymeric nanofibers: merely routine chemistry or a real challenge? Macromol. Rapid Commun. 31 (2010) 1317–1331.
[40] S. Agarwal, A. Greiner, J.H. Wendorff, Electrospinning of manmade and biopolymer nanofibers-progress in techniques, materials, and applications, Adv. Funct. Mater. 19 (2009) 2863–2879.
[41] S. Ramakrishna, K. Fujihara, W.E. Teo, T. Yong, Z.W. Ma, R. Ramaseshan, Electrospun nanofibers: solving global issues, Mater. Today 9 (2006) 40–50.
[42] J. Lin, X. Wang, B. Ding, J. Yu, G. Sun, M. Wang, Biomimicry via electrospinning, Crit. Rev. Solid State Mater. Sci. 37 (2012) 94–114.
[43] N. Ghosh, B. Kiskan, Y. Yagci, Polybenzoxazines—new high performance thermosetting resins: synthesis and properties, Prog. Polym. Sci. 32 (2007) 1344–1391.
[44] H.-C. Liu, W.-C. Su, Y.-L. Liu, Self-assembled benzoxazine-bridged polysilsesquioxanes exhibiting ultralow-dielectric constants and yellow-light photoluminescent emission, J. Mater. Chem. 21 (2011) 7182–7187.
[45] C.F. Wang, Y.C. Su, S.W. Kuo, C.F. Huang, Y.C. Sheen, F.C. Chang, Low-surface-free-energy materials based on polybenzoxazines, Angew. Chem. Int. Ed. 45 (2006) 2248–2251.
[46] C.-F. Wang, Y.-T. Wang, P.-H. Tung, S.-W. Kuo, C.-H. Lin, Y.-C. Sheen, F.-C. Chang, Stable superhydrophobic polybenzoxazine surfaces over a wide pH range, Langmuir 22 (2006) 8289–8292.
[47] B. Li, B. Jiang, D.J. Fauth, M.L. Gray, H.W. Pennline, G.A. Richards, Innovative nano-layered solid sorbents for CO_2 capture, Chem. Commun. 47 (2011) 1719–1721.
[48] Y. Li, W. Xiao, K. Xiao, L. Berti, J. Luo, H.P. Tseng, G. Fung, K.S. Lam, Well-defined, reversible boronate crosslinked nanocarriers for targeted drug delivery in response to acidic pH values and *cis*-diols, Angew. Chem. 124 (2012) 2918–2923.
[49] J. Yuan, X. Liu, O. Akbulut, J. Hu, S.L. Suib, J. Kong, F. Stellacci, Superwetting nanowire membranes for selective absorption, Nat. Nanotechnol. 3 (2008) 332–336.
[50] R.N. Wenzel, Resistance of solid surfaces to wetting by water, Ind. Eng. Chem. 28 (1936) 988–994.
[51] A. Cassie, S. Baxter, Wettability of porous surfaces, Trans. Faraday Soc. 40 (1944) 546–551.
[52] G. McHale, N. Shirtcliffe, M. Newton, Contact-angle hysteresis on super-hydrophobic surfaces, Langmuir 20 (2004) 10146–10149.
[53] L. Zhang, Z. Zhang, P. Wang, Smart surfaces with switchable superoleophilicity and superoleophobicity in aqueous media: toward controllable oil/water separation, NPG Asia Mater. 4 (2012).
[54] C.K. Liu, K. Lai, W. Liu, M. Yao, R.J. Sun, Preparation of carbon nanofibres through electrospinning and thermal treatment, Polym. Int. 58 (2009) 1341–1349.
[55] B. Ding, M. Wang, X. Wang, J. Yu, G. Sun, Electrospun nanomaterials for ultrasensitive sensors, Mater. Today 13 (2010) 16–27.
[56] E.J. Ra, T.H. Kim, W.J. Yu, K.H. An, Y.H. Lee, Ultramicropore formation in PAN/camphor-based carbon nanofiber paper, Chem. Commun. 46 (2010) 1320–1322.
[57] S.N. Arshad, M. Naraghi, I. Chasiotis, Strong carbon nanofibers from electrospun polyacrylonitrile, Carbon 49 (2011) 1710–1719.
[58] K. Chakrabarti, P. Nambissan, C. Mukherjee, K. Bardhan, C. Kim, K. Yang, Positron annihilation spectroscopy of polyacrylonitrile-based carbon fibers embedded with multi-wall carbon nanotubes, Carbon 44 (2006) 948–953.
[59] H. Niu, J. Zhang, Z. Xie, X. Wang, T. Lin, Preparation, structure and supercapacitance of bonded carbon nanofiber electrode materials, Carbon 49 (2011) 2380–2388.
[60] K.K.H. Wong, M. Zinke-Allmang, J.L. Hutter, S. Hrapovic, J.H. Luong, W. Wan, The effect of carbon nanotube aspect ratio and loading on the elastic modulus of electrospun poly (vinyl alcohol)-carbon nanotube hybrid fibers, Carbon 47 (2009) 2571–2578.
[61] Y. Yang, A. Centrone, L. Chen, F. Simeon, T.A. Hatton, G.C. Rutledge, Highly porous electrospun polyvinylidene fluoride (PVDF)-based carbon fiber, Carbon 49 (2011) 3395–3403.
[62] C.R. Nair, Advances in addition-cure phenolic resins, Prog. Polym. Sci. 29 (2004) 401–498.
[63] K. Acatay, E. Simsek, C. Ow-Yang, Y.Z. Menceloglu, Tunable, superhydrophobically stable polymeric surfaces by electrospinning, Angew. Chem. Int. Ed. 43 (2004) 5210–5213.
[64] S. Wu, S. Yin, H. Cao, Y. Lu, J. Yin, B. Li, Glucosan controlled biomineralization of $SrCO_3$ complex nanostructures with superhydrophobicity and adsorption properties, J. Mater. Chem. 21 (2011) 8734–8741.
[65] Y. Xue, H. Wang, D. Yu, L. Feng, L. Dai, X. Wang, T. Lin, Superhydrophobic electrospun POSS-PMMA copolymer fibres with highly ordered nanofibrillar and surface structures, Chem. Commun. (2009) 6418–6420.
[66] C. Huang, X. Fu, J. Liu, Y. Qi, S. Li, H. Wang, The involvement of integrin β1 signaling in the migration and myofibroblastic differentiation of skin fibroblasts on anisotropic collagen-containing nanofibers, Biomaterials 33 (2012) 1791–1800.
[67] B. Jiang, V. Kish, D.J. Fauth, M.L. Gray, H.W. Pennline, B. Li, Performance of amine-multilayered solid sorbents for CO_2 removal: effect of fabrication variables, Int. J. Greenh. Gas Control 5 (2011) 1170–1175.
[68] J. Lin, F. Tian, Y. Shang, F. Wang, B. Ding, J. Yu, Facile control of intra-fiber porosity and inter-fiber voids in electrospun fibers for selective adsorption, Nanoscale 4 (2012) 5316–5320.
[69] T.-H. Kao, J.-K. Chen, C.-C. Cheng, C.-I. Su, F.-C. Chang, Low-surface-free-energy polybenzoxazine/polyacrylonitrile fibers for bionfouling membrane, Polymer 54 (2013) 258–268.
[70] Y. Si, T. Ren, Y. Li, B. Ding, J. Yu, Fabrication of magnetic polybenzoxazine-based carbon nanofibers with Fe_3O_4 inclusions with a hierarchical porous structure for water treatment, Carbon 50 (2012) 5176–5185.
[71] C.-H. Lu, Y.-C. Su, C.-F. Wang, C.-F. Huang, Y.-C. Sheen, F.-C. Chang, Thermal properties and surface energy characteristics of

interpenetrating polyacrylate and polybenzoxazine networks, Polymer 49 (2008) 4852–4860.

[72] Y. Si, T. Ren, B. Ding, J. Yu, G. Sun, Synthesis of mesoporous magnetic Fe_3O_4@carbon nanofibers utilizing in situ polymerized polybenzoxazine for water purification, J. Mater. Chem. 22 (2012) 4619–4622.

[73] T. Ren, Y. Si, J. Yang, B. Ding, X. Yang, F. Hong, J. Yu, Polyacrylonitrile/polybenzoxazine-based Fe_3O_4@carbon nanofibers: hierarchical porous structure and magnetic adsorption property, J. Mater. Chem. 22 (2012) 15919–15927.

[74] M. Inagaki, Y. Yang, F. Kang, Carbon nanofibers prepared via electrospinning, Adv. Mater. 24 (2012) 2547–2566.

[75] Y. Ertas, T. Uyar, Main-chain polybenzoxazine nanofibers via electrospinning, Polymer 55 (2014) 556–564.

[76] Y. Ertas, T. Uyar, Cross-linked main-chain polybenzoxazine electrospun nanofibers by photo and thermal curing: stable at high temperatures and harsh acidic conditions, Polymer 84 (2016) 72–80.

[77] H.Y. Li, Y.Y. Lee, Y. Chang, C.H. Lin, Y.L. Liu, Fiber mats: robustly blood-inert and shape-reproducible electrospun polymeric mats, Adv. Mater. Interfaces 2 (2015) 1500065.

[78] B.D. Ratner, Blood compatibility—a perspective, J. Biomater. Sci. Polym. Ed. 11 (2000) 1107–1119.

[79] D.G. Castner, B.D. Ratner, Biomedical surface science: foundations to frontiers, Surf. Sci. 500 (2002) 28–60.

[80] T.A. Horbett, J.L. Brash, Proteins at interfaces II, in: ACS Symposium Series, vol. 602, American Chemical Society, Washington, DC, 1995.

[81] W.B. Tsai, J.M. Grunkemeier, T.A. Horbett, Human plasma fibrinogen adsorption and platelet adhesion to polystyrene, J. Biomed. Mater. Res. 44 (1999) 130–139.